Self-Supervised Learning Reveals Clinically Relevant Histomorphological Patterns for Therapeutic Strategies in Colon Cancer

Bojing Liu[1,2,+], Meaghan Polack[3,+], Nicolas Coudray[2, 4, #], Adalberto Claudio Quiros[5, #], Theodore Sakellaropoulos[2], Augustinus S.L.P. Crobach[6], J. Han J.M. van Krieken[7], Ke Yuan[5,8], Rob A.E.M. Tollenaar[3], Wilma E. Mesker[3], and Aristotelis Tsirigos[2,9,*]

[1] *Department of Medical Epidemiology and Biostatistics, Karolinska Institutet, Sweden.*
[2] *Applied Bioinformatics Laboratories, New York University Grossman School of Medicine, New York, New York, USA.*
[3] *Department of Surgery, Leiden University Medical Center, Leiden, The Netherlands.*
[4] *Department of Cell Biology, New York University Grossman School of Medicine, New York, New York, USA.*
[5] *Department of Computing Science, University of Glasgow, Glasgow, United Kingdom.*
[6] *Department of Pathology, Leiden University Medical Center, Leiden, The Netherlands.*
[7] *Department of Pathology, Radboud University Medical Center, Nijmegen, The Netherlands.*
[8] *School of Cancer Sciences, University of Glasgow, Glasgow, Scotland, UK.*
[9] *Department of Pathology, New York University Grossman School of Medicine, New York, New York, USA.*
[+,#] *authors with equal contribution*
[*] *Corresponding author: Aristotelis Tsirigos, Aristotelis.Tsirigos@nyulangone.org*

January 2024

Abstract

Self-supervised learning (SSL) automates the extraction and interpretation of histopathology features on unannotated hematoxylin-and-eosin-stained whole-slide images (WSIs). We trained an SSL Barlow Twins-encoder on 435 TCGA colon adenocarcinoma WSIs to extract features from small image patches. Leiden community detection then grouped tiles into histomorphological phenotype clusters (HPCs). HPC reproducibility and predictive ability for overall survival was confirmed in an independent clinical trial cohort (N=1213 WSIs). This unbiased atlas resulted in 47 HPCs displaying unique and sharing clinically significant histomorphological traits, highlighting tissue type, quantity, and architecture, especially in the context of tumor stroma. Through in-depth analysis of these HPCs, including immune landscape and gene set enrichment analysis, and association to clinical outcomes, we shed light on the factors influencing survival and responses to treatments like standard adjuvant chemotherapy and experimental therapies. Further exploration of HPCs may unveil new insights and aid decision-making and personalized treatments for colon cancer patients.

Keywords

Colon cancer; Histopathology; Self-supervised learning; Overall Survival; Tumor microenvironment; Bevacizumab.

Introduction

Traditionally, the diagnosis of colon cancer is confirmed by microscopic assessment of resection specimens on hematoxylin and eosin-stained (H&E) slides by pathologists. For each patient, a personalized treatment strategy is tailored through a multidisciplinary meeting, following guidelines consisting of risk assessments based on clinicopathological characteristics, including the tumor-node-metastasis (TNM) classification and additional biomarkers[1, 2, 3, 4]. However, due to an aging population and exponential biomarker research, diagnosing and predicting the prognosis of colon cancer patients can be time consuming, or complicated and resource-demanding, especially when incorporating screening for mutational variants [2, 3, 5, 6].

In modern digital pathology, scanning H&E slides into high-resolution whole slide images (WSIs) has enabled the applications of deep learning (DL)[7]. Deep convolutional neural networks, in particular, have benefited the diagnostic process, initially by minimizing inter-rater disagreement and workload[7]. In colorectal cancer, supervised DL models also showed the ability to predict molecular pathways (i.e. mutation density, microsatellite instability [MSI], chromosomal instability) and key mutations like *BRAF* and *KRAS*[8, 9]. DL even has intriguing potential in predicting complicated prognostic outcomes such as patient survival[10, 11]. Moreover, integrating multi-omic data with the associated H&E slides, i.e. multimodal data integration, led to improvements in prognostic prediction on overall survival (OS) for most cancer types[12].

Previous DL studies primarily focused on training models to extract features from WSIs under supervision of potentially extensive and time consuming human-derived annotations on slide or pixel-level, i.e. supervised learning[13, 8, 10, 12]. Self-supervised learning (SSL) on the other hand, has gained significantly increasing attention for its capacity to automatically capture image features from unlabeled data[9]. Applications of SSL models have demonstrated superior performance in various cancer classification and survival prediction tasks compared to traditional supervised learning models[14, 15, 16, 17]. Barlow Twins, an SSL model designed to learn non-redundant image features, has several advantages over other SSL learning models (e.g. contrastive learning models), including not requiring extensive batch sizes nor asymmetry between the network "twins"[18].

Despite the efficacy in decision-making, DL models are often labeled as "black boxes," posing significant challenges in terms of interpretability. Supervised attention-based multiple instance learning is a common interpretive method, enabling DL models to concentrate on informative segments within WSI according to predefined training labels[19]. Another approach involves employing unsupervised clustering algorithms to organize extracted features into clinically relevant and interpretable clusters which can be subsequently linked to diverse patient-related outcomes[20, 21, 17]. These clustering methods offer significant advantages, including the prediction of various clinical outcomes, intuitive visualization for pathologists, and interpretation and correlation with a range of molecular data.

Our objective is twofold: first, to automatically and reliably extract clinically-relevant histologic patterns from WSIs, which can be interpreted by expert pathologists, and second, to investigate the connections between these patterns and patient outcomes as well as molecular phenotypes across different treatment groups within a large clinical trial for colon cancer. To achieve this, we applied an SSL pipeline [17] involving the Barlow Twins encoder for feature extraction followed by a community detection algorithm to construct an unbiased atlas of histomorphologic phenotype clusters (HPCs). This algorithm was exclusively trained on public data from the colon adenocarcinoma cohort within The Cancer Genome Atlas (TCGA) multi-institutional database[22]. Remarkably, the identified HPCs generalized well in unseen WSIs obtained from the clinical Bevacizumab-Avastin® adjuVANT (AVANT) trial [23]. Subsequently, HPCs were linked to patient OS. An HPC-based classifier trained using TCGA data for OS, demonstrated prognostic significance in the external validation of AVANT study, even when considering key clinical and demographic factors typically employed in clinical settings. Notably, by conducting comprehensive analyses of the distinct histomorphologic features of each HPC and their associations with immune and genetic profiles, we provide insight into morphological and molecular determinants of patient survival upon different treatments (e.g. standard-of-care adjuvant chemotherapy and experimental targeted therapies). Exploring these features further could yield novel insights into other histopathology diagnostics, supporting shared decision-making and advancing personalized treatment options for colon cancer patients in the future.

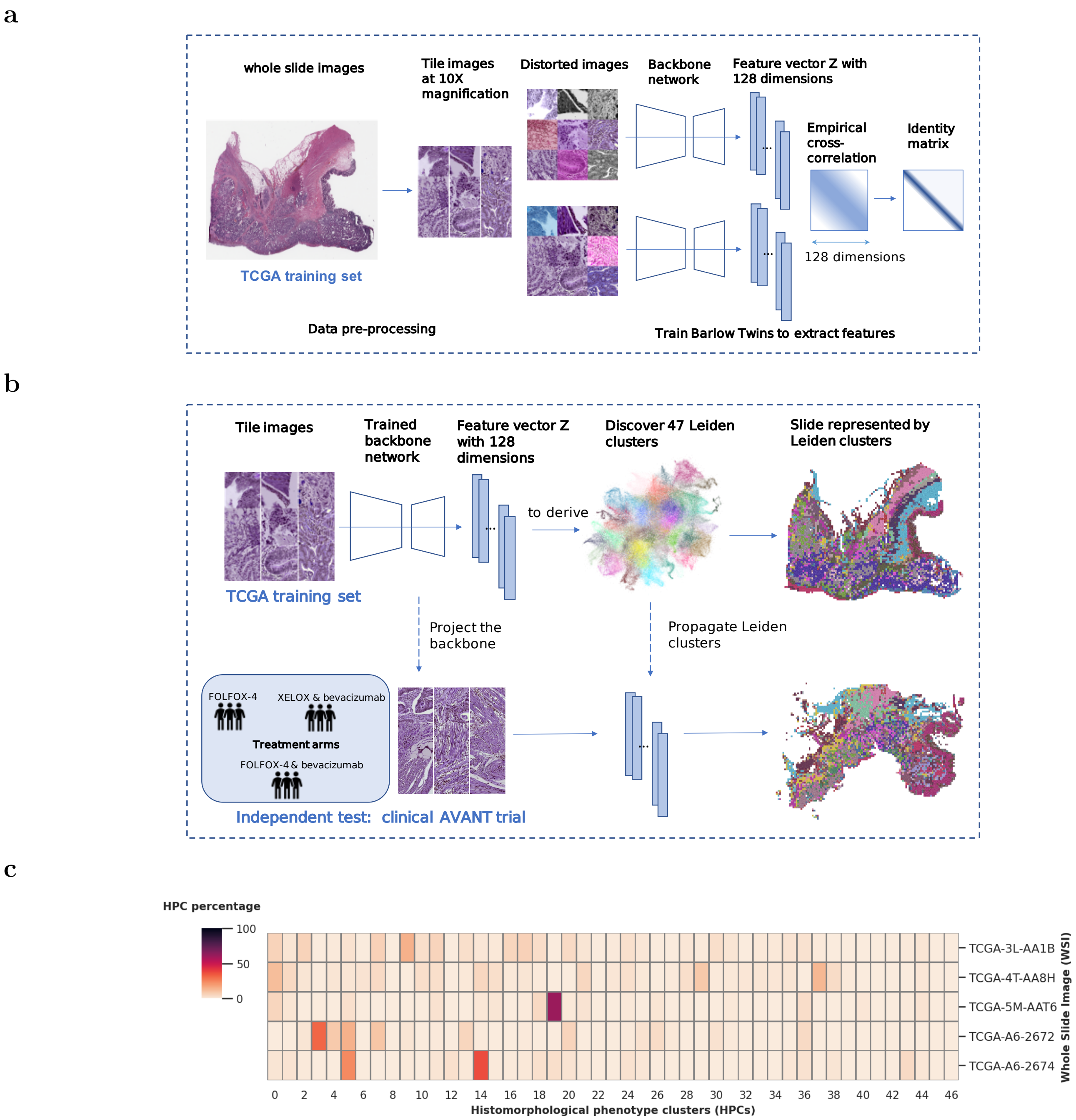

Figure 1: **Overview of the Model Architecture: Training Barlow Twins and deriving Histomorphological Phenotype Clusters.** (a) Training Barlow Twins with TCGA. WSIs from TCGA were processed to extract image tiles and normalize stain colors. The Barlow Twins network was employed to learn 128-dimensional z vectors from these image tiles. (b) Deriving HPCs. The tiles from TCGA were projected into z vector representations obtained from the trained Barlow Twins network. HPCs were defined by applying Leiden community detection to the nearest neighbor graph of z tile vector representations. Each WSI was represented by a compositional vector of the derived HPCs, indicating the percentage of each HPC with respect to the total tissue area. The Barlow Twins model and HPCs were then projected and integrated into the external AVANT trial. (c) Whole Slide Image Representation. The compositional HPC data represented the WSIs in the study. AVANT, Bevacizumab-Avastin® adjuVANT trial. HPC, histomorphological phenotype cluster. TCGA, The Cancer Genome Atlas. WSI, whole slide image.

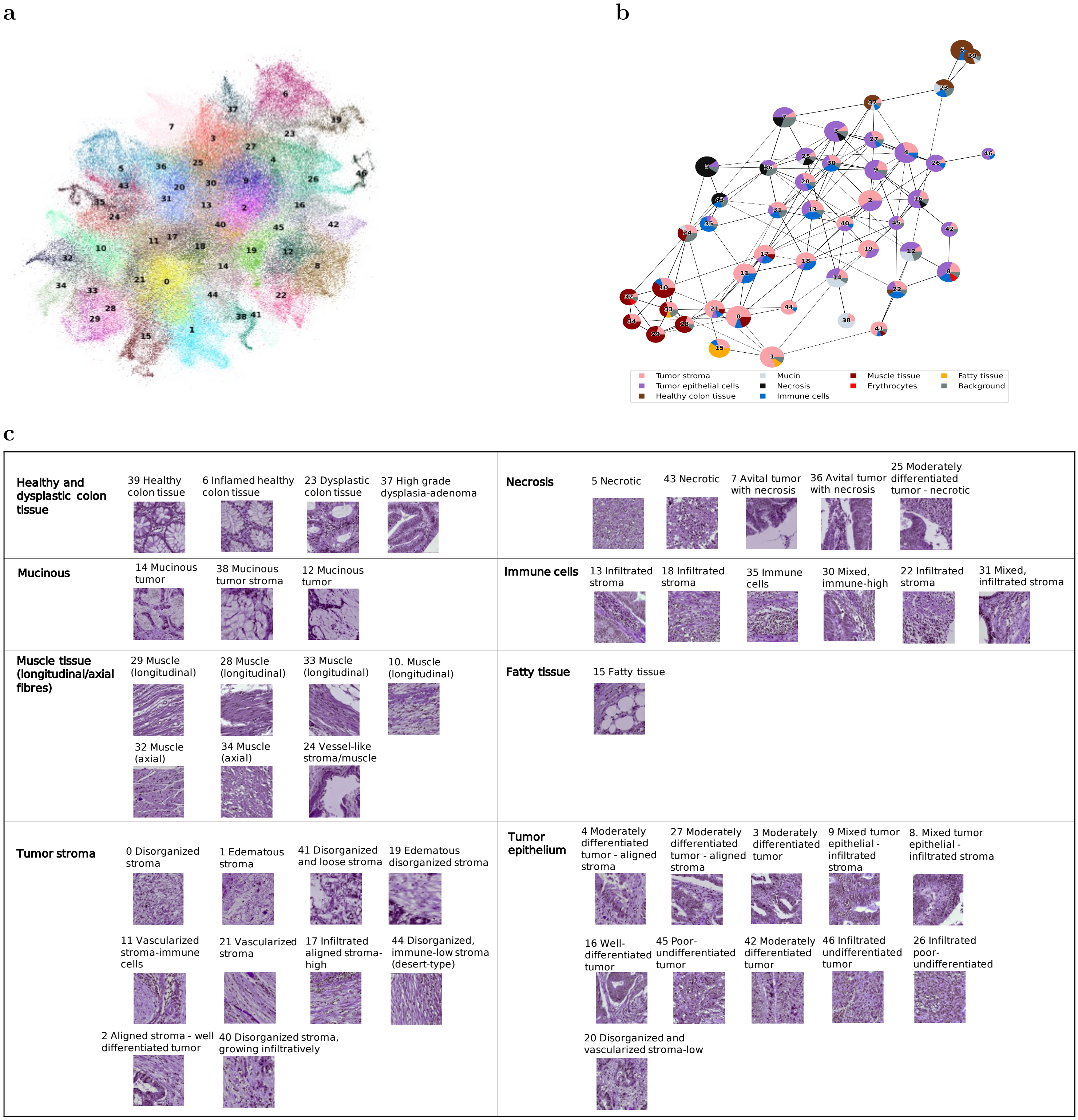

Figure 2: **Identification of HPCs in TCGA and subsequent classification into super-clusters** (a) UMAP showing 47 HPCs identified from the TCGA dataset, each scatter representing an image tile. (b) PAGA plot of HPCs. Each node represented an HPC with edges representing connections between HPCs based on their vector representation similarity. The pie chart of each node represented the tissue composition for each HPC.(c) Grouping of HPCs into super-clusters according to histopathology tissue similarities. Representative tiles for each HPC were labeled with ID and a brief description. HPC, histomorphological phenotype cluster. PAGA, partition-based abstraction graph. TCGA, The Cancer Genome Atlas. UMAP, uniform manifold approximation and projection plot

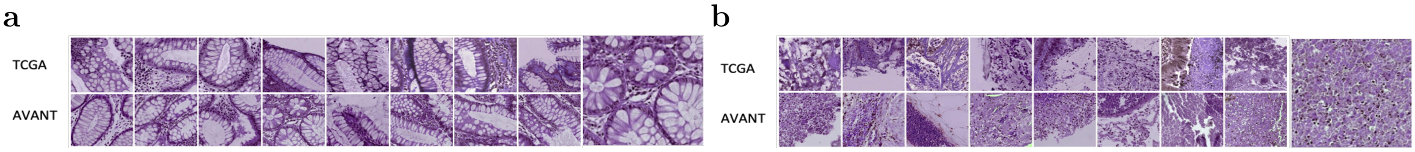

HPC 39: Healthy and dysplastic colon tissue

HPC 5:Necrosis

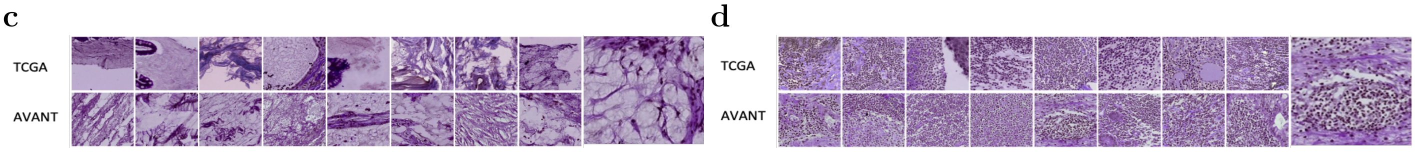

HPC 38: Mucinous tumor

HPC 35: Immune cells

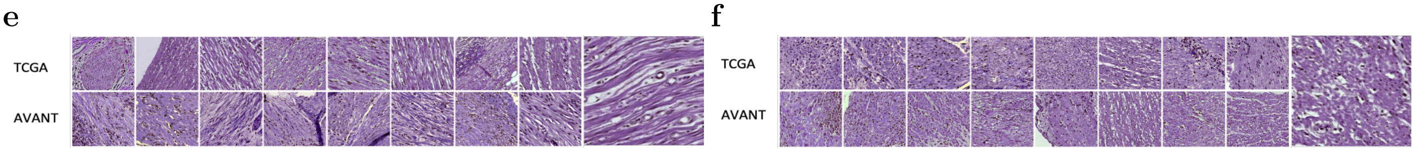

HPC 29: Muscle tissue (longitudinal)

HPC 34: Muscle tissue (axial)

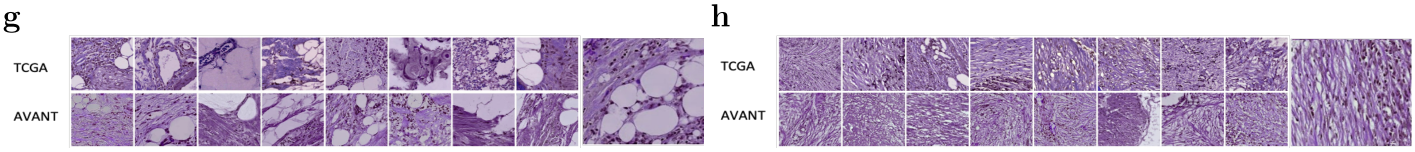

HPC 15: Fatty tissue

HPC 44: Tumor stroma

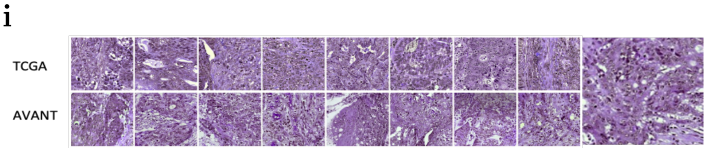

HPC 45: Tumor epithelium

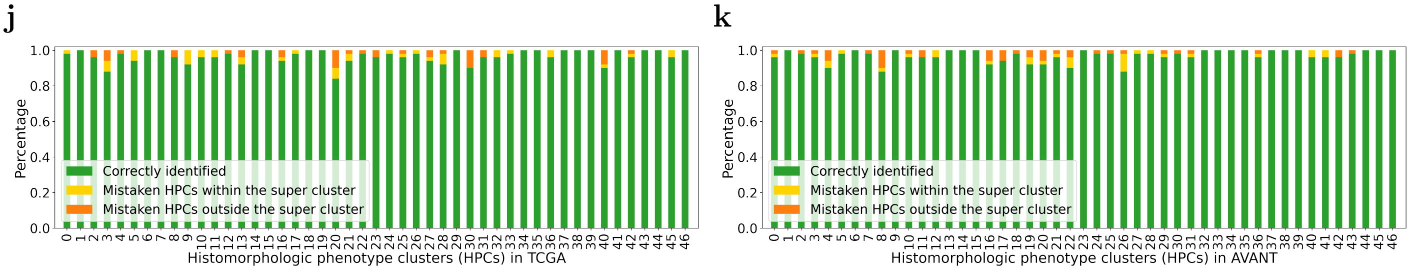

Figure 3: **Verification of HPCs in the TCGA training set and the external AVANT trial** (a-i) Example tiles from TCGA (upper row) and external clinical AVANT trial (lower row) showcase the eight super-clusters with a zoomed-in representative tile. Notably, the muscle tissue super-cluster is further divided into longitudinal and axial subgroups (j,k) Stacked bar plots illustrate instances of misclassification for each HPC in TCGA training set and AVANT external test set. Green bars represent the percentage of correctly identified odd clusters, yellow bars indicate misclassifications within the tested HPC's super-cluster, and orange bars show misclassifications outside the super-cluster. HPC, histomorphological phenotype cluster. TCGA, The Cancer Genome Atlas. AVANT, Bevacizumab-Avastin® adjuVANT trial.

Results

Self-supervised learning of WSI features using the multi-institutional TCGA dataset

We trained the self-supervised algorithm using data exclusively from the TCGA colon adenocarcinoma (TCGA-COAD) set, eliminating the need for annotations by pathologists (Figure 1). A total of 435 WSIs (428 patients) obtained from the TCGA-COAD dataset (see Methods: Study population for details) was first divided into smaller image patches (224-by-224 pixels), also known as image tiles, at a magnification level of 10x (Figure 1a) (see Online Methods: Data pre-processing for details). To identify features on these patches, we trained a SSL Barlow Twins feature extractor using a random subset of tiles (Figure 1a) (see Methods: Extracting image features using Barlow Twins for details). The Barlow Twins was trained with the objective function to evaluate the cross-correlation matrix between the embeddings (feature vector z) of two identical backbone networks, which were fed distorted variants of a batch of image tiles. The objective function was optimized by minimizing the deviation of the cross-correlation matrix from the identity matrix. This led to increased similarity among the embedding of z vectors of the distorted sample versions, while reducing redundancy among the individual components of these vectors. As a result, each tile was described as a vector of 128 extracted features that can subsequently be used to group tiles into clusters by similarity.

Construction of an unbiased atlas of histologic patterns through community detection

We applied Leiden community detection algorithm to derive HPCs, the clusters with similar histologic patterns (Figure 1b) (see Methods: Identification of Histomorphological Phenotype Clusters (HPCs) for details). The process began by first projecting the trained Barlow Twins onto the entire TCGA-COAD dataset, extracting 128-dimensional feature representations for each image tile. Subsequently, we utilized Leiden community detection on a nearest neighbor graph constructed from these tile vector representations (Figure 1b). Tiles with similar vector representations were clustered into a group and assigned a specific HPC ID number. The optimization of the Leiden configuration was achieved through an unsupervised process (see Methods: Identification of Histomorphological Phenotype Clusters (HPCs) for details, Supplementary Figure 1a), resulting in the identification of a total of 47 HPCs, visually represented in a dimensionality reduction plot (Uniform Manifold Approximation and Projection; UMAP plot) (Figure 2a).

As external dataset, we analyzed a total of 1213 colon cancer patients with pathology diagnostic H&E WSIs (one WSI per patient), a subset of the clinical AVANT trial[23, 24] (see Online Methods: Study population for details). We harnessed the optimized SSL Barlow Twins model to generate embeddings of the unseen AVANT WSI tiles. The assignment of identified HPCs to the unseen AVANT was achieved using the K-nearest neighbors approach. The HPC label of each tile in the AVANT data was determined based on majority votes from its K-nearest neighbors in the TCGA training set (Figure 1b). As a result, we obtained comprehensive visual representations of the WSIs where the WSI tiles are colored by their corresponding HPC (Figure 1b). Additionally, we were able to capture the characteristics and heterogeneity of WSIs using the compositional data derived from the HPCs, i.e. the percentage of the area on a WSI covered by each HPC, thus facilitating downstream analyses and modeling (Figure 1c).

Histopathological assessment and characterization of HPCs

Each HPC underwent histopathological analysis on a randomly selected set of 32 tiles per cluster within TCGA, independently evaluated by two pathologists (ASLPC and JHJMvK) and a researcher (MP)(see Online Methods: Interpretation of HPCs for details). Tissue types, as observed on the tiles, were described with specific attention to tumor epithelium, tumor stroma and immune cells. Other unique histopathological features or patterns, such as tumor differentiation and stromal organization, were noted as well. All present tissue types were scored in percentages (Supplementary Table 1) and depicted using pie charts (Figure 2b). We plotted the interconnections of 47 HPCs using partition-based graph abstraction (PAGA)[25], with the pie charts reflecting their tissue compositions (Figure 2b). Interestingly, distinct larger groups of clusters, or "super-clusters", could be observed based on the similarity of tissue composition, interconnectedness, and topology of HPCs in the PAGA plot (Figure 2b).

In total, we identified eight super-clusters: (1) healthy and dysplastic colon tissue, (2) necrosis, (3) mucinous areas, (4) immune cells, (5) muscle tissue (longitudinal/axial), (6) fatty tissue, (7) tumor stroma, and, (8) tumor epithelium, in no particular order, formed by groups of HPCs shown in Figure 2c. Common histopathological characteristics were noted among HPCs within each designated super-cluster, while HPCs encompassing varied tissue types across multiple super-clusters were often situated at their intersections. For instance, HPC 12, containing not only tumor epithelium but also mucinous tumor, was located between HPCs belonged to the two super-clusters of mucinous tumor and tumor epithelium in the PAGA plot. Moreover, HPC 23 marked by dysplastic colon tissue formed a bridge between the healthy colon tissue HPC 39 and the tumor epithelium-containing super-cluster HPCs, suggesting a chronological pathogenesis. In summary, the derived HPCs displayed distinctive histopathologic characteristics. Moreover, HPCs located in close proximity on the UMAP and PAGA plot, based on the extracted features, demonstrated common traits,hinting at potential pattern relationships, mixed phenotypes, or pathogenic trajectories.

Assessment of HPC consistency within and across TCGA and AVANT cohorts

Although SSL methods have been applied recently in histopathology, there is usually no systematic analysis of consistency of the histologic patterns discovered by these methods within and across datasets [15, 20]. Here, we address this potential pitfall by incorporating several qualitative and quantitative assessments.

First, qualitative assessment was conducted to evaluate the within-cluster and between-cluster heterogeneity of 47 HPCs derived in TCGA-COAD. Based on 32 randomly selected tiles from each HPC in the TCGA-COAD, three experts (ASLPC, JHJMvK, and MP) independently assessed each HPC by comparing tissue type quantity and architectures (histopathological assessment procedure stated above). Overall, all raters reached the general consensus that there was a noteworthy level of within-cluster morphological similarity and a significant diversity among the 47 HPCs (Figure 3 [a-i]), although phenotypic similarities varied across HPCs, implying that some HPCs may appear more similar than others. To delve deeper into the within-cluster and between-cluster heterogeneity, we carried out quantitative objective blinded tests within TCGA and AVANT tiles separately. This was to ascertain whether the morphological patterns identified by each HPC could also be recognized by human experts. In this test, the assessor (MP) was shown three groups of five tiles each. Two groups were from the same HPC, and the third was from a randomly selected other HPC, also called the "odd HPC". The assessor was required to identify the "odd HPC" (Supplementary Figure 2a, see Online Methods: Pathologist asessment of HPCs, for details). Each of the 47 HPCs underwent 50 tests to determine the success rate. Within TCGA, we found that 17 out of the 47 HPCs achieved 100% identification rate, while the remaining 30 HPCs had a correct identification percentage ranging from 84% to 98%. Similarly, within in AVANT, 17 out of 47 HPCs achieved the perfect accuracy, while the rest had accuracy ranging from 88% to 98% (Figure 3j). In general, HPCs in close proximity to each other in the PAGA plot or belonging to the same super-cluster were more prone to erroneous assignment.

To evaluate the effectiveness of transferring morphological patterns from the TCGA to the external AVANT test set, three experts (ASLPC, JHJMvK, and MP) independently reviewed a randomly chosen set of 32 tiles from the TCGA-COAD subset and another 32 tiles randomly selected from the AVANT trial. This qualitative comparison concluded a remarkable resemblance between the TCGA and AVANT tiles within their respective HPCs (Figure 3 [a-i]). In comparing the objective test results from TCGA and AVANT, we found an 80% overlap in the misclassified HPCs between the two datasets and 65% overlap in correctly classified HPCs. These results indicate that the robust morphological features extracted from the training set can be effectively transferred to an independent unseen test set.

HPC-based classifier was associated to OS in patients treated with standard-of-care and AVANT-experimental treatment

We explored the prognostic significance of HPCs on OS. The OS prediction model was developed within TCGA-COAD (see Online Methods: Identification of Histomorphological Phenotype Clusters (HPCs), for details). For external validation, we utilized the control group from the AVANT trial who had only received standard adjuvant chemotherapy (i.e. FOLFOX-4). The AVANT trial aimed to investigate whether combining bevacizumab, a humanized anti-vascular endothelial growth factor (VEGF) monoclonal antibody, with standard chemotherapy would improve survival among colon cancer patients[26, 23]. The trial had three treatment arms: FOLFOX-4, bevacizumab+FOLFOX-4, bevacizumab+XELOX. The study was prematurely terminated due to the adverse effect in patient survival associated with bevacizumab[23]. Given the unique bevacizumab experimental treatment and its adverse effects, we hypothesized that the survival model trained on TCGA-COAD patients may not generalize well in the AVANT bevacizumab-treated group. We referred to our source population, represented by the TCGA-COAD, as the "standard-of-care group", in contrast to the unique bevacizumab treatment

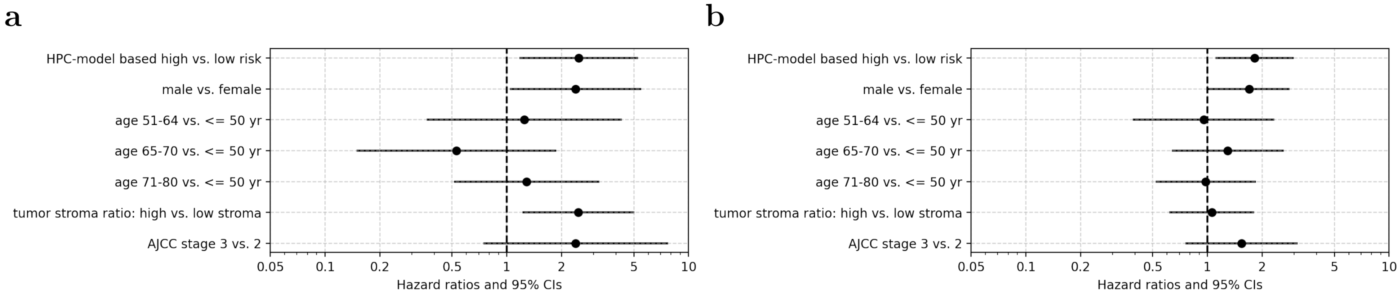

Standard-of-care group: external test set of AVANT control group

AVANT experimental group

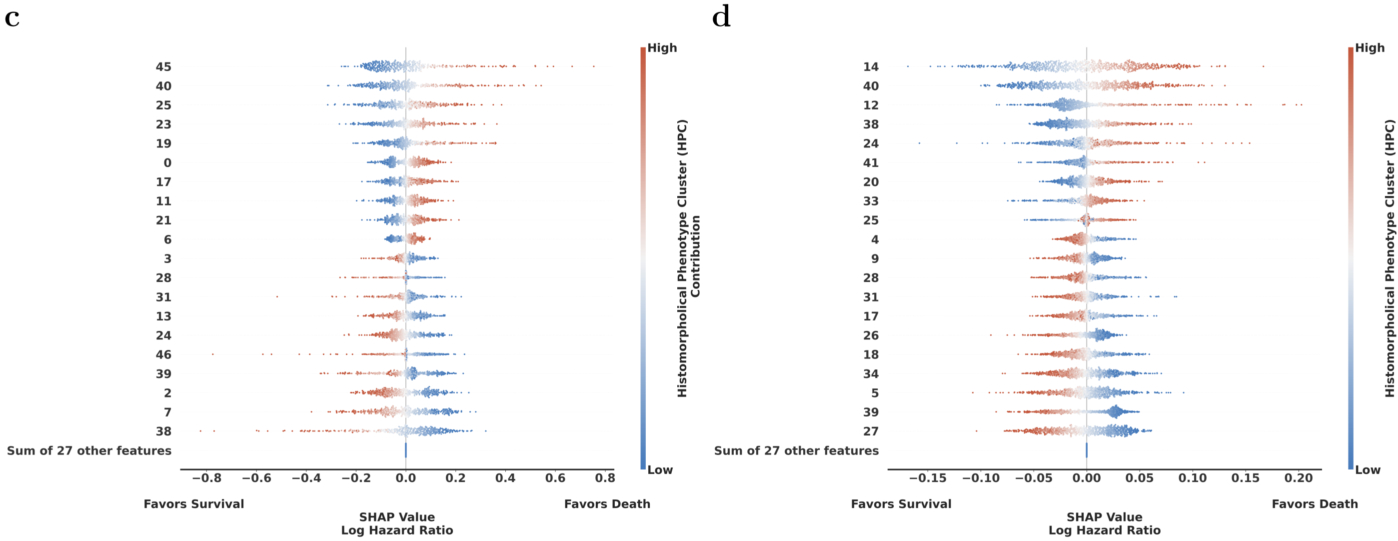

Top 20 OS-associated HPCs trained in standard-of-care TCGA

Top 20 OS-associated HPCs trained in AVANT experimental groups

Figure 4: **HPC-based classifier was associated with OS in patients treated with standard-of-care and AVANT-experimental treatment.** (a) Ordinary Cox regression for OS, incorporating the HPC-based risk classifier, along with sex, age categories, tumor-stroma ratio, and AJCC TNM staging, was conducted within the external test set of the AVANT control group. The HPC model-based classifier stands as an independent prognostic factor (HR 2.50, 95% CI 1.18-5.31) for OS. (b) Ordinary Cox regression for OS, incorporating the HPC-based risk classifier, along with sex, age categories, tumor-stroma ratio, and AJCC TNM staging, was conducted within the AVANT experimental group. The HPC model-based classifier stands as an independent prognostic factor (HR 1.82, 95% CI 1.11-2.99) for OS. (c and d) The SHAP summary plots depict the relationship between the center-log-transformed compositional value of an HPC and its impact on death hazard prediction. The color bar indicates the relative compositional value of an HPC, with red indicating higher and blue indicating lower composition. Higher compositions of the top 10 HPCs were associated with worse OS, while higher compositions of the bottom 10 HPCs were linked to improved OS. AJCC TNM, American Joint Committee on Cancer tumor-node-metastasis classification. AVANT, Bevacizumab-Avastin® adjuVANT trial. HPC, histomorphological phenotype cluster. OS, overall survival. SHAP, SHapley Additive exPlanations. TCGA, The Cancer Genome Atlas.

in the AVANT trial. We then opted to validate the OS prediction model, trained on TCGA-COAD data, primarily on AVANT patients who exclusively received standard FOLFOX-4 chemotherapy. This subset is henceforth referred to as the "AVANT control group", serving as an independent test set for validation.

We modeled HPCs on OS using Cox regression with L2 regularization trained within the TCGA-COAD incorporated all 47 HPCs as predictors. The model was optimized through five-fold cross-validation (CV) on the TCGA training set (see Online Methods: Identification of Histomorphological Phenotype Clusters (HPCs), for details). The optimized regularized Cox model was then tested in the independent test set of the AVANT control group. We observed the test set c-index of 0.65 (bootstrap 95% confidence interval [CI] 0.55-0.74) (Supplementary Figure 3b). The HPC-based classifier (i.e. high risk versus low risk) was determined by the median predicted hazard obtained in the TCGA-COAD. The HPC-based model also outperformed a clinical baseline model trained on age, sex, tumor-stroma ratio (TSR), and AJCC stage (Supplementary Figure 3c). To investigate whether HPC-based classifier provides additional prognostic value to the existing important clinical predictors, a regular multivariable Cox regression was fitted within the external AVANT control test set. The model included HPC-based classifier as well as important clinical and demographic variables (Figure 4a). Notably, the HPC-based risk classifier demonstrated significance as an independent prognostic factor (hazard ratio [HR] 2.50, 95% CI 1.18-5.31), along with male sex (HR 2.42, 95% CI 1.07-5.47) and the TSR (HR 2.49, 95% CI 1.23-5.04). The 20 most important HPCs associated to OS were summarized using the interpretable SHapley Additive exPlanations (SHAP) (Figure 4c).

Harnassing the well-defined experimental protocols in AVANT, we were granted the unique opportunity to examine the influence of HPCs on colon cancer OS in the bevacizumab treatment groups (i.e. bevacizumab+FOLFOX-4 or bevacizumab+XELOX). Given the proven comparable therapeutical efficacy of FOLFOX-4 and XELOX [26, 27, 28], we consolidated the bevacizumab+FOLFOX-4 and bevacizumab+XELOX cohorts into a unified "AVANT-experimental group". Similar to the analysis stated above, we trained Cox regressions with L2 regularization encompassing all 47 HPCs within the AVANT-experimental patients using 5-fold CV (see Online Methods: Identification of Histomorphological Phenotype Clusters (HPCs) for details). The HPC-based classifier remained of independent prognostic value (HR 1.82, 95% CI 1.11-2.99) after adjusting for age, sex, tumor staging, and TSR (Figure 4b). The top 20 most influential HPCs on OS prediction were shown in the SHAP summary plot (Figure 4d).

Pathological assessment of OS-associated HPCs in the standard-of-care and AVANT-experimental group groups

We highlighted the top 20 most influential HPCs on OS prediction reflecting the SHAP summary plot (Figure 4c, 4d) in the PAGA plots for the standard-of-care and AVANT-experimental groups (Figure 5). The survival-favorable HPCs were highlighted in a shade of red and the survival-unfavorable HPCs were highlighted in blue. Preliminary findings showed that HPCs containing proportionally more healthy colon tissue or immune cells appeared associated with an improved OS, and HPCs comprising mucinous tumor, tumor stroma, and poor-to-undifferentiated tumor epithelium were associated with worse OS in both groups.

The healthy colon tissue-containing HPC 39 was among the top survival-favorable HPCs indicated by larger SHAP values in both groups (Figure 4c, 4d). In the standard-of-care group, HPC 23 characterized by dysplastic and low grade tumor epithelium and HPC 6 marked by stroma-infiltrated healthy colon tissue indicating inflammation, were associated with a worse OS. HPC 31, predominately composed of immune cells, was associated with an improved OS in both treatment groups. A similar association was also noted for immune-mixed HPC 13, which is part of the immune super-cluster, in the standard-of-care group (Figure 5a) as well as HPC 18 (aligned stroma-immune cells) and HPC 17 (aligned stroma with immune component) in the AVANT-experimental group (Figure 5b). In the AVANT-experimental group, the mucinous super-cluster (HPCs 12, 14 and 38) was associated with a poor survival (Figure 5b), while conversely, HPC 38 (mucinous tumor stroma) led to a better survival in the standard-of-care group (Figure 5a)

Upon closer examination, we noted that the algorithm captured a distinction in stroma organization within the stromal tissue presented in the tumor stroma and tumor epithelium super-clusters. HPCs in these two super-clusters all contained some component of stromal tissue. However, HPCs with disorganized or heterogeneous tumor stroma with neovascularization (HPC 40 in both groups; 0, 11 and 21 in standard-of-care, and 41 in the AVANT-experimental group) were associated with a poor survival, whereas aligned and organized tumor stromal "strands" were often observed among the top survival-favorable HPCs (HPC 2 in the standard-of-care and HPC 27 in the AVANT-experimental group).

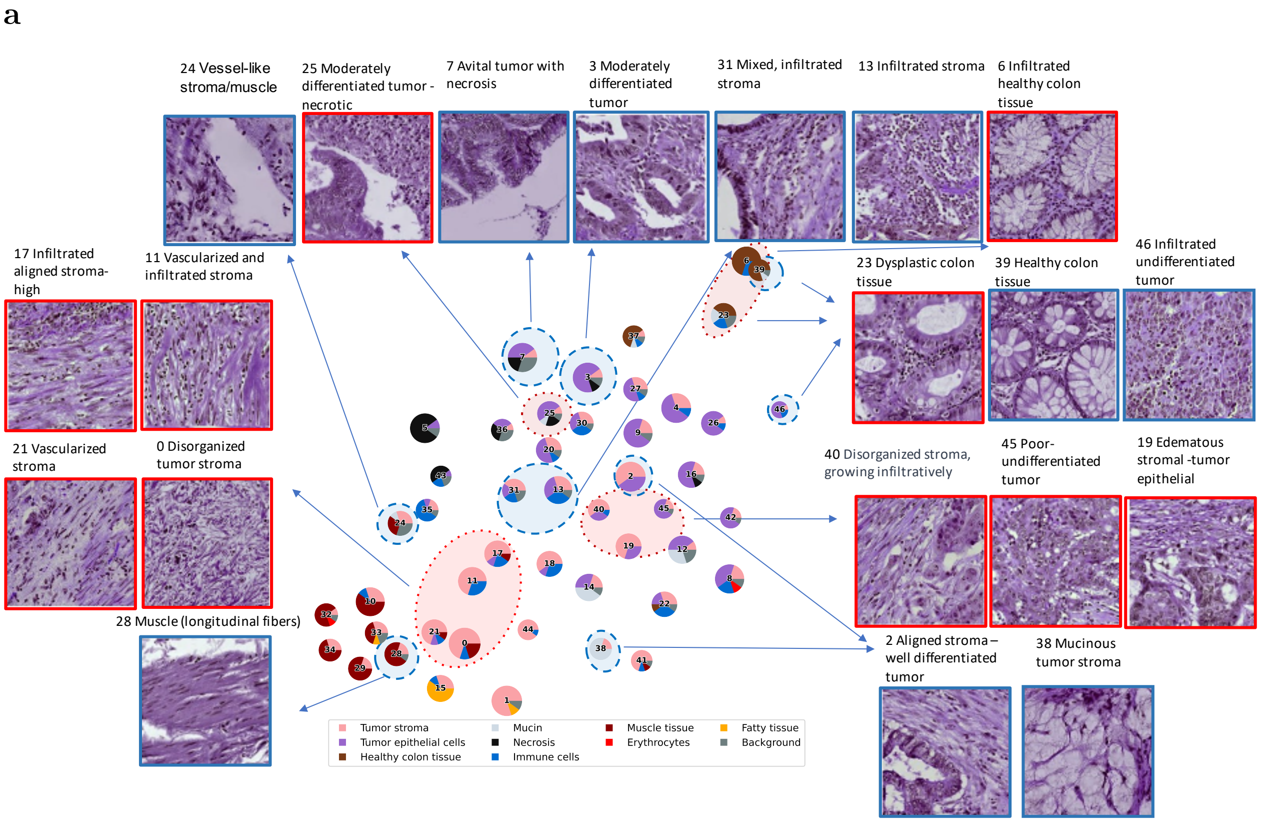

Top 20 OS-related HPCs in the standard-of-care group

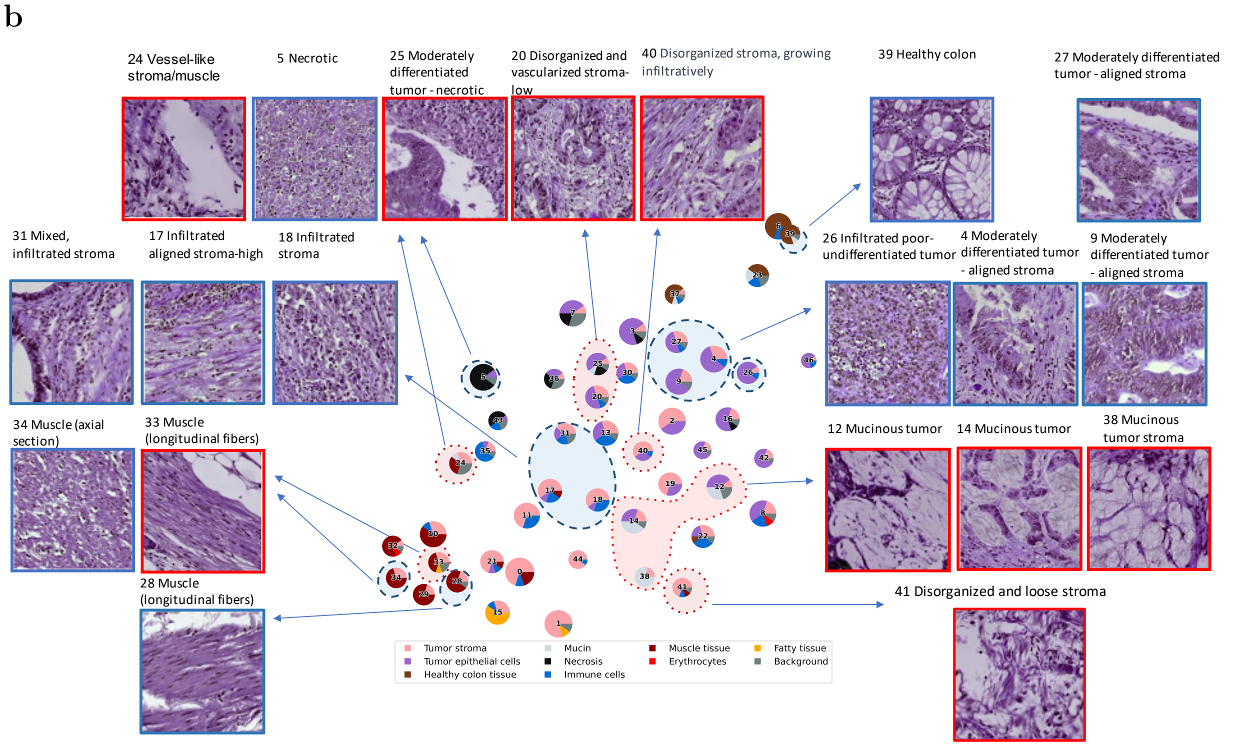

Top 20 OS-related HPCs in the AVANT-experimental group

Figure 5: **PAGA plots highlighted with important HPCs related to OS in the standard-of-care and experimental treated group** (a) Standard treated group: HPCs colored in the red are linked to worse survival and HPCs colored in blue are linked to better survival. (b) AVANT-experimental treated group: HPCs colored in the red are linked to worse survival and HPCs colored in blue are linked to better survival. AVANT, Bevacizumab-Avastin® adjuVANT trial. HPC, histomorphological phenotype cluster. PAGA, partition-based graph abstraction.

Moreover, the tumor differentiation grade was another parameter correlating with HPCs and their impact on OS. Poor-to-undifferentiated tumor epithelium, e.g. HPC 45, in the standard-of-care group, was linked to a worse survival, while well-to-moderately differentiated tumor led to an improved survival (e.g. HPCs 3 in the standard-of-care group and HPC 4 in the AVANT-experimental group). A unique pattern was furthermore observed in survival-favorable HPCs 46 (standard-of-care group) and 26 (AVANT-experimental group), which was characterized by a predominance of poor-to-undifferentiated tumor epithelium but accompanied by a notable influx of immune cells.

Additional findings were related to the survival-favorable HPC 7 (avital tumor epithelium) in the standard-of-care group (Figure 5a) and the positive association between necrosis-dominated HPC 5 and better survival in the AVANT-experimental group (Figure 5b). The associations between HPCs containing muscle tissue (e.g. HPC 24, 33 and 34) and survival were generally inconsistent, possibly due to the similarity of muscle fibers and tumor stroma, caused for instance by the organization of muscle fibers and vascularization.

Outcome-associated HPCs are linked to diverse immune features in the tumor microenvironment

Spearman correlation coefficients were calculated between the top 20 survival-related HPCs on one hand, and the TCGA immune landscape on the other hand (see Methods for details). The correlation heatmap was plotted with bi-directional hierarchical clustering (Figure 6a). Interestingly, in the standard-of-care group (Figure 6a), HPCs 0, 11, 17 and 21, all part of the phenotypic tumor stroma super-cluster, were identified by the genotypic immune analysis as having a positive correlation with the stroma-high category. Moreover, their SHAP values indicated an positive association with worse survival. Conversely, HPCs 13 and 31 in the immune cell super-cluster were correlated with higher leukocyte fraction. Survival prediction model suggested the immune cell super-cluster was in general associated with a better survival. Further anticipated findings included the validation of HPCs 2 and 24, marked by stroma-high tiles, through immune feature correlation within the stroma high category.

In the AVANT-experimental group (Figure 6b), survival-favorable HPCs 5, 17, 31, 18 correlated with an increased leukocyte fraction. Notably, HPCs 17 and 31 aligned with an elevated immune cell composition (Figure 5b). Additionally, HPCs 17 and 18 were also associated with a higher expression of stroma, which was consistent with the observed stroma-high morphology (Figure 5b). On the contrary, survival-unfavorable HPCs 14, 40 and 20 exhibited higher genomic instability. For instance, HPCs 40 and 20 were positively correlated with homologous recombination defects, intratumor heterogeneity, and HPC 14 was positively linked to nonsilent mutation rate, single nucleotide variants and indel neoantigens. Although HPC 14 also showed a positive correlation with the leukocyte fraction, a more pronounced association with genomic instability through multiple pathways seemed to play a greater role in its negative impact on OS.

The resulting correlations with immune landscape data aligned with the observed morphologies of HPCs, particularly in stromal and immune features. Furthermore, the data suggest a potential role in genomic instabilities within the AVANT-experimental group. Taken together, these results demonstrate that HPCs can capture the remarkable heterogeneity of the tumor microenvironment.

Outcome-associated HPCs are linked to oncogenic pathways and bevacizumab's mechanism of action

Next, we performed gene set enrichment analysis (GSEA) to discern associations between top OS-related HPCs from both the standard-of-care and AVANT-experimental groups and key cancer hallmark pathways (Figure 6c and d). In the AVANT-experimental cohort, survival-related HPCs showed striking alignment with the enrichment observed in oncogenic hallmark pathways (Figure 6d), which such alignment was overall much less pronounced in standard-of-care group (Figure 6c). Still, in the standard-of-care group, pathways encoding epithelial-to-mesenchymal transition, leading to an increased tumor-stromal percentage, were enriched in survival-unfavorable HPCs 11, 17, 40 and 19. HPCs related to inflammatory response pathways showed primarily positive associations with OS, e.g. with HPCs 13 and 31 related to better survival.

In the AVANT-experimental group (Figure 6d), we observed a strong correlation between hierarchical clustering based on oncogenic enrichment scores and survival-related HPCs. Several HPCs exhibited enrichment in pathways that potentially be specific to bevacizumab through its target of VEGFa expression and *KRAS* signaling-up pathway. HPC 5, characterized by necrosis, was linked to elevated VEGFa expression (rho=0.163, P=0.005), indicating patients with higher pre-treatment necrosis levels may benefited from the bevacizumab treatment. HPC 27, 18, and 31 were associated with enriched

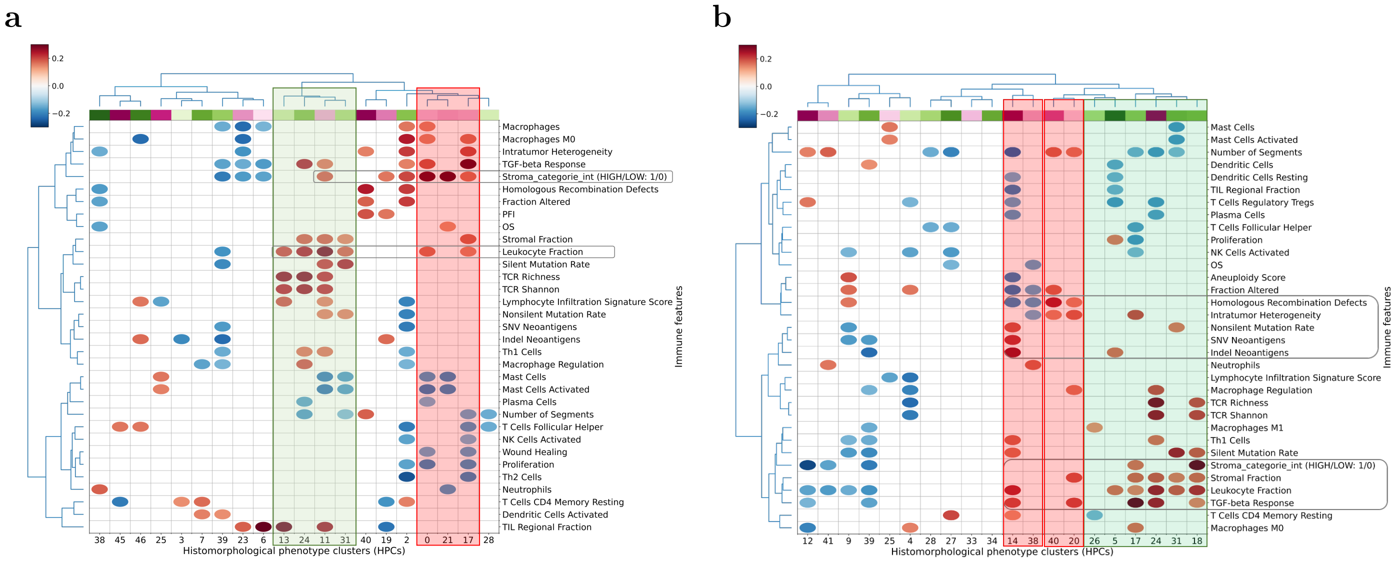

Standard-of-care group: immune landscape

AVANT-experimental group: immune landscape

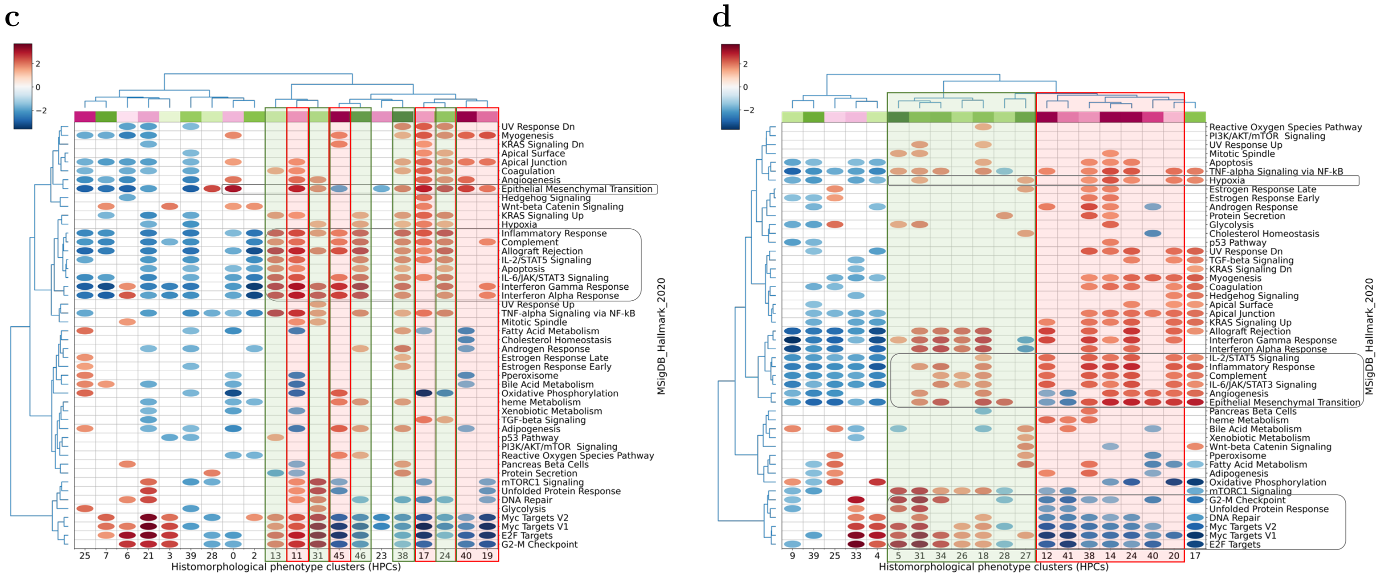

Standard-of-care group: GSEA analysis

AVANT-experimental group: GSEA analysis

Figure 6: **Survival-associated HPCs in relation to immune and genetic profile.** (a) Standard-of-care group: Spearman's correlations between top 20 OS-related HPCs and immune landscape features. HPCs (columns of the matrix) were colored according to the beta-coefficients estimated from the optimized regularised Cox regression, with red indicating HPCs related to worse survival and green indicating HPCs related to better survival. The color bar at the upper left corner indicates the value of correlation coefficients with red denoting positive and blue denoting negative correlations. (b) AVANT-experimental treated group: Spearman's correlations between top 20 OS-related HPCs and immune landscape features. (c) Standard-of-care group GSEA between the top OS-related HPCs and major cancer hallmark pathways. HPCs (columns of the matrix) were colored according to the beta-coefficients estimated from the optimized regularised Cox regression, with red indicating HPCs related to worse survival and green indicating HPCs related to better survival. The color bar at the upper left corner indicates the value of the correlation coefficients with red denoting enrichment and blue denoting underrepresentation in a gene pathway. (d) AVANT-experimental treated group GSEA for the top 20 OS-related HPCs. AVANT, Bevacizumab-Avastin® adjuVANT trial. GSEA, gene set enrichment analysis. HPC, histomorphological phenotype cluster. OS, overall survival.

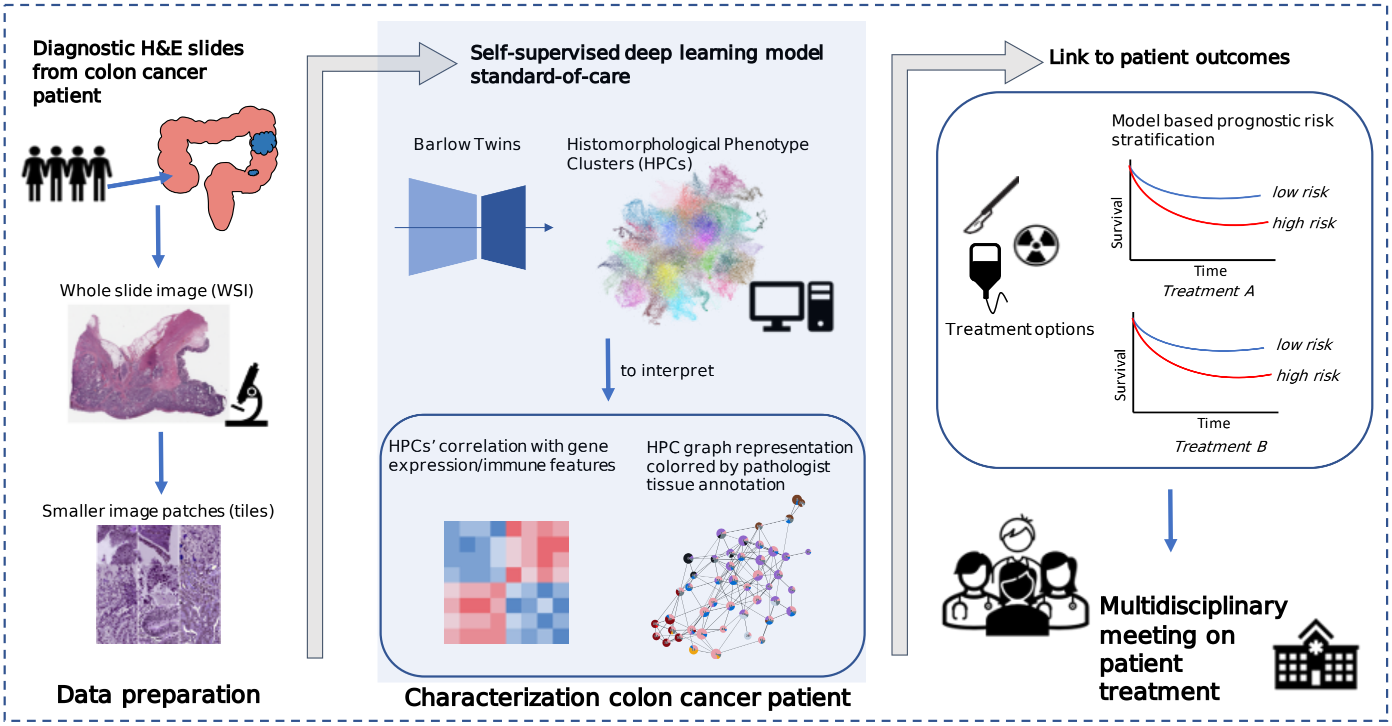

Figure 7: **Clinical application of AI-derived HPCs in prediction of patient outcomes.** The clinical algorithm consists of three key stages: data preparation, cancer patient characterization, and AI-supported multidisciplinary treatment meetings. Data preparation involves collecting histopathology WSIs, segmenting them into small image tiles. Patient characterization encompasses SSL model training, yielding HPCs via clustering. HPCs are easily interpretable by pathologists, linkable to omic data. Most importantly, HPCs are valuable for predicting diagnosis, patient outcomes, and treatment responses. In treatment-related outcomes, AI-predicted high/low risk groups aid multidisciplinary meetings, enabling personalized treatment plans by oncologists, pathologists, and physicians. AI, artificial intelligence. HPC, histomorphological phenotype cluster. SSL, self-supervised learning, WSI, whole slide image.

hypoxia (HPCs 31, 27) and angiogenesis (HPCs 18, 31), and unfolded protein (HPCs 31, 1, 5) pathways which involve the VEGFa gene. In addition, other survival-favorable HPCs may not be specific to bevacizumab but related to the standard cytotoxic chemotherapy of XELOX and FOLFOX-4. Survival-unfavorable HPCs (12, 38, 14, 24, 20) were linked to the *KRAS* signaling-up pathway, which may have a negative impact on the prognosis of patients treated with FOLFOX. Certain survival-favorable HPCs exhibited enrichment in pathways related to cell cycle regulation, signaling, DNA repair, and growth, including G2/M checkpoint (34, 31, 5), E2F targets (5, 31, 34, 26, 18), Myc targets (5, 31, 34, 26, 18), and mTORC1 signaling (5, 31, 34, 26, 18), DNA repair (18, 31). In contrast, survival-unfavorable HPCs demonstrated depletion in these pathways.

Discussion

In this study, we derived and independently validated a total of 47 distinct HPCs that were extracted from colon cancer H&E WSIs using a self-supervised algorithm. These HPCs possess distinctive histomorphologic features carefully identified and assessed by the pathologists and were also linked several immune features and oncogenic pathways. The HPCs showed state-of-the-art performance on OS prediction. Furthermore, the HPC-based risk classifier was an independent prognostic factor after adjusting for important clinical and demographic variables, suggesting additional insight beyond the current clinical prognostication. The unique AVANT trial enabled us to endeavor in identifying possible mechanisms of response to bevacizumab and standard chemotherapy using the HPCs.

Moreover, we hereby emphasize the importance of the tumor microenvironment, or tumor stroma, and its effect on survival. Tumor stroma is composed of extracellular matrix, vasculature, immune cells and cancer-associated fibroblasts, forming a complex and close interaction with tumor epithelial cells[29, 30]. Subject to increasing research the past decades, this dynamic entity has been found to modulate tumor behavior through its cross-talk, and ultimately influence patient-related outcomes. Specifically, regarding the amount of stroma and stromal architecture, i.e. alignment or categorization of the desmoplastic reaction, and immune infiltrate in the stroma, our results corroborate previous literature [31, 24, 32, 33, 34, 35].

We identified common histopathological patterns associated with survival as observed in both the standard and bevacizumab-treated group. In line with our results, immune cells (e.g. HPCs 13, 31)[36] and aligned stroma-low tumors (e.g. HPCs 2, 27)[32, 31] were associated with better survival, while poor-to-undifferentiated tumor epithelium (e.g. HPC 45) or mucinous tumor epithelium (e.g. HPCs 12, 14) [2, 3], and disorganized stroma-high tumors (e.g. HPCs 40, 0)[32, 31] were linked to worse survival. This pathological phenotype correlated with the corresponding genetic immune profile (e.g. increased leukocyte fractions correlated with HPCs 13 and 31; and a stroma-high category was see in HPCs 0, 21, 17, 11) and enrichment in oncogenic pathways (e.g. epithelial-to-mesenchymal transition pathway, contributing to tumor stroma amounts[29], correlated with HPCs 17 and 11). We also observed an association, though imperfect, between mucinous tumor, poor-to-undifferentiated tumor epithelium, and survival. One explanation may arise from the absence of contextual information in small images. The differentiation between well-differentiated and undifferentiated, or adenocarcinoma and more mucinous tumor types, is established based on whether each tissue type constitutes more than 50% of the total tumor, underscoring the importance of considering the overall context[3].

Another interesting discovery emerges from the survival-favoring HPCs 26 (AVANT-experimental group) and 46 (standard-of-care group). These HPCs contain primarily poor-to-undifferentiated tumor epithelium but with a high influx of immune cells. Such a histopathological pattern is frequently observed in MSI tumors[37]. The MSI tumors have been linked to a favorable prognosis [38, 2], characterized with lower differentiation grade, increased T-cell infiltration, and reduced susceptibility to invasiveness and *KRAS* mutation [38], however, are commonly identified through separate MSI analysis and/or additional immunohistochemical staining for mismatch repair enzymes in pathology diagnostics[3, 2, 38].

Furthermore, we also noted HPC 39 containing predominately healthy colon tissue associated with better survival. The interpretation arises from the nature of the multivariable analysis where the 47 HPCs were modeled simultaneously. One can interpret this result as, while holding the other 46 HPCs constant, patients with more abundance of healthy colon tissue showed an improved survival. The higher proportion of healthy colon tissue may indicate relatively smaller or less aggressive tumors. Indeed, within routine TNM assessments, lower pathological T-stage is known to lead to an improved survival[3].

In the GSEA analysis, we noted a remarkable concurrence in AVANT-experimental group between clustering based on cancer hallmark pathways and outcome-related HPCs, while such alignment was much less pronounced in the standard-of-care group. One possible explanation is the heterogeneity of patients in the TCGA-COAD dataset. In contrast to the well-defined treatment protocol in AVANT, TCGA-COAD patients encompass diverse disease and demographic profiles. Consequently, this diversity led to a wide spectrum of treatments, including surgical, neoadjuvant, and adjuvant therapies. The survival-related HPCs discovered in the TCGA-COAD could therefore be, if related at all, to multiple distinctive biological pathways. A general alignment observed in the AVANT-experimental group was therefore not anticipated in the standard-of-care group.

In the AVANT-experimental group however, several survival-favoring HPCs either directly correlated with VEGFa expression or were associated to enrichment in oncogenic pathways involving VEGFa gene, indicating a favorable responses to the contentious bevacizumab treatment. In particular, HPC 5, primarily characterized by necrosis, emerged as a significant contributor to enhanced survival, displaying a positive correlation with VEGFa expression, which is the target of bevacizumab. Necrosis promotes the expression of VEGFa, as dying tumor cells release signals that stimulate the growth of new blood vessels [26]. In addition, survival-favoring HPCs 18, 27, and 31 were associated with enriched hypoxia and angiogenesis pathways which also involve the VEGFa gene. We hypothesize that patients exhibiting a higher abundance of HPC 5, 18, 27, and 31 may correspondingly express elevated levels of VEGFa, the target of bevacizumab, which in turn result in a more favorable response to this treatment.

Oxaliplatin plus 5-fluorouracil-based regimens of XELOX and FOLFOX-4 are standard chemotherapy for colorectal cancer[39]. Nonetheless, the treatment response is still modest with an estimate rate of approximately 50% [1, 39], and the prediction of which patients will respond to this adjuvant chemotherapy remains challenging. We observed enrichment in oncogenic pathways that may be within the context of XELOX and FOLFOX-4 treatments in the AVANT trial. Survival-unfavorable HPCs (12, 38, 14, 24, 20) were linked to the *KRAS* signaling-up pathway. In line with previous literature, several KRAS mutations activate downstream signaling pathways and the *KRAS G12D* mutation was predictive of an inferior response to FOLFOX [40]. Interestingly, HPCs 12, 14, and 38 contained mutinous tumors tissue, which has also been linked to *KRAS* mutational burden [37, 41]. Survival-favoring HPCs (5, 31, 34, 26, 18, 27) were associated with enrichment in pathways of cell cycle, signalling, DNA repair, and growth (i.e. G2/M checkpoint, E2F targets, Myc targets, and mTORC1 signaling), while survival-unfavorable HPCs (12, 41, 38, 14, 24, 40, 20) linked to a depletion of those pathways. Interestingly, patients with altered DNA repair capacity showed greater benefits from treatment with oxaliplatin[39]. Moreover, carriers of MNAT1 gene, which is one of the leading genes in the G2/M checkpoint pathway[42], were linked to better treatment outcome of FOLFOX[39]. A plausible mechanism is that patients exhibiting activated oncogenic activities within these pathways might harbor a greater abundance of targets suitable for oxaliplatin-based cytotoxic chemotherapy.

Another finding was our HPC-based prediction on OS outperforming the clinical baseline model. This HPC-based risk classifier remained an independent prognostic factor (HR 2.50, 95% CI 1.18-5.31) after adjusting for crucial clinical and demographic variables including TSR and tumor stage. This finding aligns with recent findings reported by Jiang et al. [11]. Interestingly, although both HPCs and TSR were derived from H&E slides, they appeared to encapsulate distinct non-overlapping information. A potential explanation could be that the HPC-based classifier captures intricate details, while TSR assessment requires a broader contextual understanding, not fully attainable with small image patches [31]. Comparing our OS prediction directly with previous studies poses further challenges due to differences in cancer types (e.g., colorectal [10, 43, 11] instead of colon cancer only), varied outcomes (e.g., 5-year disease-free survival [DFS] [10]), diverse statistical measures (e.g., hazard ratio [43]), and absence of independent test sets[12] in prior studies. Nevertheless, a recently study reported a test set c-index of 0.65 for OS prediction in colorectal cancer[11] aligning with our reported c-index in the context of colon cancer.

Building upon the aforementioned findings, this study showcases the prospective clinical utility of AI-generated HPCs (Figure 7). Cancer WSIs were preprocessed into image patches and subsequently used to train SSL encoders and to form HPCs. These HPCs serve as condensed representations of the original WSIs, ready to be inspected by pathologists and enabling flexible linkage to molecular data. These HPCs hold promise in classifying tumor characteristics, potentially predicting patient prognosis and discerning distinct sensitivity groups to various therapies. In turn, this prediction can aid decision-making in future multidisciplinary meetings. Moreover, this algorithm operates in a self-supervised manner, affording enhanced transferability among datasets, flexible linkage to multimodal omics data, and broader applicability across various outcome domains.

Despite the interesting findings, the study also has several limitations. The identification of HPCs was based on small image tiles as is imperial to model training, while information regarding the larger context is likely lost, as also stated above. For example, it is often challenging to distinguish aligned and organized tumor stromal 'strands' from muscle tissue through traditional microscopic assessment [44]. Therefore, pathologists typically make this distinction based on contextual cues, color variances, or use additional immunohistochemical stainings, all of which is not available within the small image patches. Another limitation pertains to using TCGA as the training set. Although the TCGA is a large open sourced database, it depends on the availability of registered clinicopathological data. This introduces potential bias and variability in data quality across participating institutions. Moreover, due to data availability, we were only able to focus on predicting OS rather than DFS which may better reflect tumor behavior and biology[22, 45]. Lastly, due to the AVANT treatment regimen design, separate analysis regarding bevacizumab or oxaliplatin-based chemotherapy was not attainable. Nonetheless, we made efforts to differentiate between their distinct mechanisms by conducting histopathological inspections and correlating the findings with immune landscape and oncogenic pathways.

In conclusion, our study employed a self-supervised approach to identify and validate histopathological features in colon cancer that are recognizable by human eyes and relevant to prognosis. These features were interpreted through a pathology-focused perspective. Our results highlighted the clinical significance of tumor tissue type, stromal amount and architecture, and the involvement of immune cells. Integration of histopathological features with genetic and gene expression data unveiled potential insights into oncogenic pathways and their relation to patient survival. Utilizing data from the clinical AVANT trial, we proposed mechanisms influencing patient sensitivity to diverse treatments. Future research should focus on refining prediction accuracy and validating the proposed mechanisms regarding the therapeutic strategies in colon cancer.

Methods

Study population

The TCGA-COAD dataset was used for training and extracting features and histologic patterns using SSL. This dataset consisted of 451 WSIs from 444 unique patients[22] with matched genetic and transcriptomic information. We excluded duplications and WSIs with erroneous resolution that were not suitable for the analyses (i.e. only several kilobytes in size). The final TCGA training set included 435 WSIs from 428 patients with a diagnosed pathological TNM-stage I-IV colon carcinoma (333 alive, 94 dead, and 1 missing vital status). We referred to the source population which TCGA-COAD representing as the "standard-of-care" group, contrasting it with the clinical trial data described below.

As external dataset we leveraged a study comprising 1213 colon cancer patients with available diagnostic H&E WSIs (one WSI per patient) as part of the clinical Bevacizumab-Avastin® adjuVANT (AVANT) trial[23, 24]. Bevacizumab, a humanized anti-vascular endothelial growth factor (VEGF) monoclonal antibody, had initially been shown to improve the OS in patients with metastatic colon cancer when jointly used with the standard chemotherapy[26]. In the phase III AVANT trial, with an intent-to-treat population of 3451 patients, an open-label design was used[23]. Patients were randomly assigned in a 1:1:1 ratio to three different treatment regimens: FOLFOX-4 (intravenous 5-fluorouracil/folinic acid plus oxaliplatin), bevacizumab-FOLFOX-4, and bevacizumab-XELOX (oral capecitabine plus intravenous oxaliplatin)[23]. The study aimed to investigate whether adding bevacizumab to the standard oxaliplatin-based adjuvant chemotherapy could improve DFS among patients with stage II-high risk and III colon cancer[23]. However, the trial was prematurely terminated due to the serious adverse effect on the patient's OS in the bevacizumab-treated group[23]. The AVANT trial was chosen also due to the previously studied potential correlation of VEGF, the stromal compartment (e.g. the TSR), and patient prognosis[24, 32, 31]. For a detailed overview of the trial and patient characteristics, see Zunder et al[24].

Given the unique treatment regimen of bevacizumab and its adverse effect in non-metastatic colon cancer, as also proven by a predecessing clinical trial, the NSABP protocol C-08 trial [46], we decided to primarily validate OS prediction, trained in the TCGA-COAD, within the control group who only received FOLFOX-4 (without bevacizumab) and refer to it as the "AVANT control group". Subsequently, as several phase III trials had demonstrated that FOLFOX and XELOX are comparable in the context of metastatic colorectal cancer[26, 27, 28], we thus combined the bevacizumab+FOLFOX-4 and bevacizumab+XELOX groups into a unified "AVANT-experimental group" and conducted a separate analysis to predict OS within the bevacizumab-treated patients.

The present study was performed by using anonymized archival material, not necessitating new informed consent. Archival material was derived from the AVANT-trial (BO17920), performed in accordance with the declaration of Helsinki[23, 24]. Protocol approval was obtained from the local medical ethics review committees or institutional review boards at participating sites.

Data pre-processing

Tissue segmentation and image tiling

We used the preprocessing methods described in our previous study[47]. Tissue areas in WSIs were segmented against background at 10x magnification level (pixel size approximate 1.0 um). WSIs were divided into non-overlapping image tiles of size 224x224 pixels. The selection of a 10x magnification was based on two key considerations. Firstly, it aligns with the standard magnification utilized by pathologists during microscopic assessments in clinical practice. Secondly, we conducted visual inspections of tiles at 20x, 10x, and 5x magnifications, and found that tiles at 10x magnification provided an optimal balance of capturing sufficient detail while also offering a reasonably sized overview of the morphological structure. In addition, to overcome the variability of color stains from different scan facilities in the TCGA and AVANT cohorts, we further applied the color normalization[48]. In total, we obtained 1,117,796 tiles in the TCGA training set (i.e. TCGA-COAD), and 4,827,055 tiles in the AVANT external test set (AVANT-COAD, consisting of the standard and experimental treatment groups).

Extracting image features using Barlow Twins

We trained the SSL Barlow Twins feature extractor based on 250,000 image tiles randomly selected from the TCGA-COAD dataset. The Barlow Twins extracted unique latent vectors (128 dimension) from the preprocessed image tiles in TCGA. The model is based on ResNet-like architecture consisted of several ResNet layers and one self-attention layer[17]. In essence, the Barlow Twins calculates the cross-correlation matrix between the embedding outputs of two identical twin networks, both fed with distorted versions of the same image tile[18]. It is optimized to make the correlation matrix close to the identity matrix[18]. We used the batch size of 64 trained on a single NVIDIA® Tesla V100 GPU for 60 epochs. The Barlow Twins feature extractor was frozen after the training and used to project image tiles into latent representation in the entire TCGA training set.

To facilitate the downstream analysis, we also applied five-fold CV partition in the TCGA-COAD training set on patient level balanced the on American Joint Committee on Cancer (AJCC) TNM stage, survival outcomes (i.e. death or censor), and binned survival time categories.

Leiden community detection algorithm

The Leiden clustering algorithm is a graph-based clustering algorithm that aims to identify distinct communities or clusters within graph data [49]. In brief, it optimizes the modularity function (Equation 1), in such way to maximize the difference between the actual number of edges and the expected number of edges in a community[49]. This modularity function also includes a resolution parameter γ, with higher values leading to more clusters and lower values leading to fewer clusters. Leiden clustering is initiated by assigning each node in the graph to its own individual cluster, treating them as separate communities, then iteratively optimizes the modularity function by moving a node from its current cluster to a neighboring cluster or by merging clusters until the algorithm converged and revealing distinct communities or clusters. We employed the Leiden clustering in a particular workflow. We began by constructing a neighborhood graph using the K=250 nearest neighbors from a pool of 200,000 randomly selected latent image vectors from a training set. Subsequently, we applied the Leiden algorithm to identify clusters within this neighborhood graph. These cluster labels were then propagated to each individual image tile across the entire dataset, once more utilizing the K-nearest neighbors approach.

$$\mathcal{H} = \frac{1}{2m}\sum_{c}\left(e_c - \gamma\frac{K_c^2}{2m}\right) \tag{1}$$

Modularity measures the difference between the actual number of edges in a community and the expected number of such edges. e_c denotes the actual number of edges in community c and the expected number of edges is expressed as $\frac{K_c^2}{2m}$, where K_c is the sum of the edges of the nodes in community c and m is the total number of edges in the network. γ is the resolution parameter, with higher values leading to more clusters and lower values leads to fewer clusters.

Identification of Histomorphological Phenotype Clusters (HPCs)

We identified HPCs as clusters obtained from the Leiden community detection algorithm operated on 128-dimensional image features extracted through the Barlow Twins encoder. The Leiden method was also used for quality control to eliminate artifacts and underfocused image tiles. Quality control was carried out after training the Barlow Twins and extracting image features. In the overall process, we initially generated a substantial number of Leiden clusters. Next, we visually examined sample image tiles from each cluster and removed clusters exhibiting artifacts such as air bubbles, foreign objects, etc., or those containing under-focused images. In particular, within the training set of a randomly selected CV fold (fold 0), we randomly selected 200,000 latent image vectors to generate Leiden clusters. We obtained 125 clusters at a high resolution of $\gamma = 6$. The Leiden labels were propagated into the entire TCGA set using again the KNN methods. Next, we inspected randomly selected sample tiles (N=32) from each cluster and identified 12 clusters containing predominately artifacts or underfocused images. Image tiles labelled by these 12 clusters were subsequently removed from the further analyses. The HPCs were newly derived in this cleaned dataset by re-running the Leiden clustering. Optimization of the HPCs was conducted using primarily unsupervised methods and secondarily confirmed using supervised methods. Importantly, both the two approaches converged on the same optimal Leiden resolution, as elaborated below.

Optimization of HPCs using unsupervised methods

Leiden resolutions (i.e. $\gamma = 0.4$, 0.7, 1.0, 1.5, 2.5, and 3.0) were optimized using three unsupervised statistical tests: the Disruption score, Silhouette score, and Daves-Boundin index. Due to the potentially high variance in data from the different institutions in the TCGA, all three scores were weighted by the mean percentage of the institution presence in each cluster. We consistently identified the optimal Leiden resolution as 1.5 through the three aforementioned statistical tests (Supplementary Figure 1a).

Optimization of HPCs and the prediction of overall survival (OS) using Cox regressions with L2 regularization

To identify optimal HPC configurations and their associations with patient OS, we trained L2 regularized Cox regressions for OS prediction using 5-fold CV. The Cox regressions were trained separately among standard-of-care colon cancer patients (i.e. TCGA-COAD) and among the AVANT-experimental group.

OS prediction in the standard-of-care group Prediction of OS from HPCs among the standard-of-care group was trained within TCGA-COAD using 5-fold CV and tested in the independent AVANT control group. Specifically, for each CV fold within TCGA-COAD, we began by generating a range of Leiden clustering configurations at various resolutions, including gamma values of 0.4, 0.7, 1.0, 1.5, 2.5, and 3.0, using the method described earlier. Next, at each Leiden resolution, we calculated the compositional representation of HPCs for each WSI (see Main Figure 1c), followed by a center-log-ratio transformation (Equation 2). This transformation was designed to mitigate inter-dependencies among HPCs, ensuring that the independence assumptions required for subsequent Cox regression analysis were met. The L2 regularized Cox regressions were then trained at the patient level, with one WSI per patient considered. At each Leiden resolution, we performed a multivariable L2 regularized Cox regression, incorporating all center-log-ratio-transformed HPCs specific to that resolution. We fine-tuned L2 regularizer (alpha) through an iterative process involving 50 steps, spanning the alpha range from 10^{-4} to 10^{4}. This sequence of steps was repeated across all five cross-validation folds. The optimal Leiden resolution and L2 regularizer was selected based the CV C-index.

Through this optimization process, the optimal Leiden resolution was determined to be 1.5, and the L2 regularizer alpha was fixed at 0.1842.Of the note, this optimal Leiden resolution of 1.5 concurred with the result from the unsupervised approaches. An HPC-based classifier was determined by the median predicted hazard obtained in the TCGA-COAD. Once the Cox model is optimized, we evaluated the final model performance in the external test set consisting of the AVANT-standard care group.First, the 47 HPCs were integrated into the AVANT-standard care group by employing the K-nearest neighbors method (K=250), where each AVANT tile's HPC label was determined based on the majority votes from its nearest neighbors in the TCGA training set. Next, the trained Cox model, with optimized regularization and parameter estimates for the HPCs, was then applied to the AVANT-standard care group to test the prediction of OS (Supplementary Figure 2b).

Furthermore, employing the same CV method, we trained a clinical baseline model on OS in TCGA-COAD using L2 regularized Cox regression incorporating age, sex, TNM staging, and TSR as predictors. We observed a c-index of 0.58 (bootstrap 95% CI 0.49-0.67) in the independent AVANT AVANT-standard care group and the model-based risk classifier did not reach the statistical significance level (Supplementary Figure 2c). This baseline model illustrates a simulation of decision-making in clinical practice as control, using the most readily available and relevant clinical and demographic variables. Our HPC-based model outperformed this clinical baseline model. In addition, we explored whether the HPC-based classifier add additional prognostic value to the existing important clinical predictors. We fitted an ordinary multivariable Cox regression within the external AVANT-standard care group, including HPC-based classifier, sex, age, tumor-stroma ratio, and AJCC stage (Supplementary Figure 2d).

$$\mathrm{clr}(x_i) = \ln\left(\frac{x_i}{g}\right), x_i = \frac{\text{counting of tiles in } C_i}{\text{total number of tiles in each WSI}}, \quad g = \left(\prod_{i=1}^{n} x_i\right)^{\frac{1}{n}} \tag{2}$$

The center-log-ratio transformation (clr) calculates the natural logarithm of the ratio (x_i) of compositional data for a specific cluster (C_i) to the geometric mean (g) of the compositional data across all clusters. The compositional data (x_i) is obtained by dividing the counting of tiles in cluster C_i by the total number of tiles in each WSI. The geometric mean (g) is computed by multiplying the compositional data values (x_i) for each cluster (C_i), ranging from $i = 1$ to n (where n is the total number of clusters), and raising the resulting product to the power of $\frac{1}{n}$.

OS prediction in the AVANT-experimental group

Bevacizumab, a unique intervention investigated in the AVANT trial, was unlikely accessed by patients from the TCGA-COAD cohort. Considering the significant poor prognostic outcome associated with bevacizumab in non-metastatic colorectal cancer, we postulated that the relationship between HPCs on OS might be influenced by this intervention. Furthermore, we hypothesized that estimates of HPCs on OS trained from the general COAD population, such as TCGA, might not be applicable to bevacizumab-treated patients.

To address these hypotheses, we conducted a separate 5-fold CV estimating the relationship between HPCs and OS within the bevacizumab-treated patients (AVANT-experimental group). Similarly, we generated 5-fold train-validation split stratified by TNM stage and survival time. We used the same sets of HPCs obtained at the previously optimized Leiden 1.5 resolution. Similarly, we modelled the center-log-transformed compositional data of HPCs on OS using Cox regressions with L2 regularization. We fine tuned the L2 regularizer specifically for AVANT-experimental group. The model performance of HPCs on OS prediction was evaluated using c-index in the 5-fold CV validation sets.

To understand the importance of each HPC on OS, we employed SHAP values[50]. SHAP values measure the marginal contribution of a HPC towards the predicted OS, considering all possible combinations of features. We highlighted top 20 important HPCs favoring and hindering survival for both standard-of-care and AVANT-experimental treated COAD patients.

Interpretation of HPCs

Plotting HPCs using UMAP and PAGA plot

We applied UMAP dimensionality reduction [51] to TCGA-COAD tile vector representations (128-dimensional vectors), color-coded by 47 HPC IDs using optimized Leiden clustering configuration from the prior step. Next, we generated a PAGA plot where each HPC is a node connected by lines based on vector similarity. Pie charts within each HPC node showed annotated tissue type percentages annotated independently by three experts (ASLPC, JHJMvK, and MP) (see below). We analyzed this plot to identify and describe significant interconnected clusters (see Main Figure 2b). Based on the PAGA plot, we also defined the "super-clusters" according to the interconnections among HPCs and tissue composition (see Main Figure 2b).

Pathologist assessment of HPCs

Histopathological assessment and characterization of HPCs The histomorphological features of 47 HPCs derived in TCGA training set were comprehensively and independently analyzed by two expert pathologists (ASLPC and JHJMvK) and one medical researcher (MP). The analysis was exclusively conducted using image tiles and the assessors were kept blinded to results from other analyses. Specifically, we randomly selected a set of 32 tiles from each HPC within TCGA and each individual tile was examined with specific focus on tumor epithelium, tumor stroma, and immune cells. Attention was also paid to general tumor differentiation grade, tumor stromal amount, stromal classification, i.e. aligned or disorganized, stromal neovascularization or other notable patterns (e.g. dysplastic tissue, fatty tissue, muscle tissue fibers, blood vessels, erythrocytes, etc.)[3, 32, 44]. Each assessor evaluated the tissue composition based on 32 randomly selected tiles per HPC, providing an average tissue composition for each HPC. In cases of conflicting tissue annotations, the assessors carried out discussions to achieve consensus. In addition, a short label was given to each HPC based on tissue annotation either according to the first and second predominant tissue types and patterns (e.g. "aligned stroma - well differentiated tumor epithelium"), or as the single most dominant tissue type covering $\geq$70% area of an average tile (e.g. "necrotic"). The tissue description, composition, and short labels of all 47 HPCs were displayed in Supplementary Table 1.

Assessment of HPC consistency within and across TCGA and AVANT cohorts We performed various qualitative and quantitative analyses to evaluate the within-cluster and between-cluster heterogeneity of HPCs, as well as their transferability from TCGA to AVANT cohorts. Initially, qualitative visual assessments were independently conducted by three experts (ASLPC, JHJMvK, and MP) to evaluate the concordance within and discordance between HPCs. This evaluation followed the established protocol for tissue type analysis, utilizing the previously randomly selected 32 tiles per HPC. The assessors noted consistent histomorphological patterns within HPCs and diverse patterns across various HPCs.

In addition, we conducted quantitative objective tests within TCGA and AVANT tiles seperately to determine if the learned morphological features of the HPCs could be replicated by human eyes. We displayed three rows, each containing five tiles, which is referred to as a "question". Among these rows, two belonged to the same HPC, while the third row, also referred to as the "odd HPC", were tiles randomly selected from a different HPC. All example tiles were randomly selected within each HPC. The researcher (MP) was required to identify the "odd HPC", and upon doing so, the next question was presented (example shown in Supplementary Figure 2). In order to calculate the success rate, we ran 50 questions per HPC and we repeated the experiment for all 47 HPCs. The test was conducted on a closed website accessible through login and was conducted seperately for tiles randomly selected from TCGA and AVANT. The conducted experiment exhibited an average completion time of under 10 seconds per question. The success rate was determined for each HPC by dividing the number of incorrect answers by the total number of questions (50 questions per HPC). We hypothesized that most HPCs would be distinguishable. However, some HPCs may be challenging to differentiate due to tissue similarities, either within the same super-cluster or through similar tissue morphology (e.g., muscle tissue and tumor stroma). The results showed that HPCs in close proximity to each other in the PAGA or belonging to the same super-cluster were indeed more prone to being mistaken.

To validate HPCs derived from the TCGA training set were generalized well in the external AVANT test set, three assessors independently carried out visual examination of tissue characteristics in 32 randomly selected tiles from each HPC in both the AVANT trial and the TCGA set, comparing their histomorphological features regarding tissue types and composition established in the previous step. Assessors confirmed that the consistent and meaningful patterns learned by the Barlow Twins, could be replicated across other clinical cohorts like the AVANT trial. To validate our observation, we compared the objective test results between TCGA and AVANT, focusing on the overlap in both misclassified and correctly classified HPCs across the datasets.

Linkage between survival-related HPCs, immune landscape, and gene expression data

We calculated Spearman correlations between HPCs and RNASeq-derived immune features from TCGA-COAD data, correcting for false discovery rate (0.05) using Benjamini-Hochberg correction. We created bi-hierarchical clusters for immune features and top 20 significant HPCs linked to OS in both standard-of-care and AVANT-experimental groups. Clustering was based on correlation coefficients using Euclidean distance and Ward's aggregation.

In addition, we performed GSEA to explore the potential associations between HPCs and the major cancer hallmark pathways, as previously described [52]. The analysis was conducted within 282 TCGA-COAD patients with available gene expression data for 20,530 genes. For each HPC, we calculated the

Spearman correlation coefficients with the expression data of these 20,530 genes and sorted the resulting correlation coefficients to rank the genes in a descending order. Subsequently, enrichment scores for 50 major cancer hallmark pathways, as defined by the "MSigDB_Hallmark_2020" gene set [42], were computed for each HPC based on the generated ranked gene list. A positive enrichment score indicated higher composition of a HPC was associated with gene enrichment in a pathway and a negative value suggested higher composition of a HPC was associated with underrepresentation of a pathway. We plotted the cancer hallmark enrichment scores for the top 20 important HPCs related to OS, for both the general and experimental treatment groups. We set a significance level of 0.01 of the false discovery q value. The analysis was conducted using the gseapy (1.0.4) Python package. Two-way hierarchical clustering was based on the Euclidean distance of the enrichment scores and Ward's aggregation method.

Code and data availability

All data analyses are based upon publicly available Python software packages and codes are available from our previous publication (https://github.com/AdalbertoCq/Histomorphological-Phenotype-Learning)[17]. The data that support the findings of this study are available from Genentech Inc., Roche but restrictions apply to the availability of these data, which were used under licence for the current study, and so are not publicly available. Data are however available from the authors upon reasonable request and with permission of Genentech Inc., Roche.

Acknowledgements

The work is supported by the Swedish Research Council (BL, 2019-06360), NCI/NIH Cancer Center Support Grant (AT, P30CA016087), and the Bollenstreekfonds, Lisse, Netherlands (WEM). We thank the team of NYU Langone High Performance Computing (HPC) Core's resources supporting us to perform the analysis. We would like to thank the NYU Applied Bioinformatics Laboratories (ABL) for providing bioinformatics support and helping with analysis of the data. ABL is a shared resource partially supported by the Cancer Center Support Grant P30CA016087 at the Laura and Isaac Perlmutter Cancer Center. We would also like to thank Leslie Solorzano for her input in data preprocessing. The AVANT-trial (BO17920) was originally financed by Genentech Inc., Roche, Switzerland. The authors thank Nikolas Jan Rakebrandt as liaison from Roche.

Author contributions

B.L. executed data processing, model training, and data analyses. A.C.Q., N.C., and B.L. wrote python codes used to run all the experiments. M.P. and W.E.M. provided coordination in obtaining H&E slides and corresponding data from Bevacizumab-Avastin® adjuVANT trial. M.P., A.S.L.P.C, J.H.J.M.v.K, provided histological assessment and interpretation of HPCs. B.L. and M.P. wrote the first draft of the manuscript which was later revised and approved by all co-authors. B.L., N.C., A.C.Q, T.S., A.T. provided expertise in deep learning, biostatistics, and bioinformatics. M.P., A.S.L.P.C, J.H.J.M.v.K, R.A.E.M.T, and W.E.M provided expertise in colon cancer histopathology and biology. A.T. supervised the study.

Declaration of interests

AT is a co-founder of Imagenomix. The remaining authors declare no competing interests.

References

[1] James D Brierley, Mary K Gospodarowicz, and Christian Wittekind. *TNM classification of malignant tumours*. John Wiley & Sons, 2017.

[2] G. Argilés, J. Tabernero, R. Labianca, D. Hochhauser, R. Salazar, T. Iveson, P. Laurent-Puig, P. Quirke, T. Yoshino, J. Taieb, E. Martinelli, and D. Arnold. Localised colon cancer: Esmo clinical practice guidelines for diagnosis, treatment and follow-up†. *Annals of Oncology*, 31(10):1291–1305, 2020.

[3] Martin R Weiser. Ajcc 8th edition: colorectal cancer. *Annals of surgical oncology*, 25:1454–1455, 2018.

[4] A Cervantes, R Adam, S Roselló, D Arnold, N Normanno, J Taïeb, J Seligmann, T De Baere, P Osterlund, T Yoshino, et al. Metastatic colorectal cancer: Esmo clinical practice guideline for diagnosis, treatment and follow-up. *Annals of Oncology*, 34(1):10–32, 2023.

[5] Eileen Morgan, Melina Arnold, A Gini, V Lorenzoni, CJ Cabasag, Mathieu Laversanne, Jerome Vignat, Jacques Ferlay, Neil Murphy, and Freddie Bray. Global burden of colorectal cancer in 2020 and 2040: Incidence and mortality estimates from globocan. *Gut*, 72(2):338–344, 2023.

[6] Aoife Maguire and Kieran Sheahan. Controversies in the pathological assessment of colorectal cancer. *World journal of gastroenterology: WJG*, 20(29):9850, 2014.

[7] Kaustav Bera, Kurt A Schalper, David L Rimm, Vamsidhar Velcheti, and Anant Madabhushi. Artificial intelligence in digital pathology—new tools for diagnosis and precision oncology. *Nature reviews Clinical oncology*, 16(11):703–715, 2019.

[8] Mohsin Bilal, Shan E Ahmed Raza, Ayesha Azam, Simon Graham, Mohammad Ilyas, Ian A Cree, David Snead, Fayyaz Minhas, and Nasir M Rajpoot. Development and validation of a weakly supervised deep learning framework to predict the status of molecular pathways and key mutations in colorectal cancer from routine histology images: a retrospective study. *The Lancet Digital Health*, 3(12):e763–e772, 2021.

[9] Veenu Rani, Syed Tufael Nabi, Munish Kumar, Ajay Mittal, and Krishan Kumar. Self-supervised learning: A succinct review. *Archives of Computational Methods in Engineering*, pages 1–15, 2023.

[10] Ellery Wulczyn, David F Steiner, Melissa Moran, Markus Plass, Robert Reihs, Fraser Tan, Isabelle Flament-Auvigne, Trissia Brown, Peter Regitnig, Po-Hsuan Cameron Chen, et al. Interpretable survival prediction for colorectal cancer using deep learning. *NPJ digital medicine*, 4(1):71, 2021.

[11] Xiaofeng Jiang, Michael Hoffmeister, Hermann Brenner, Hannah Sophie Muti, Tanwei Yuan, Sebastian Foersch, Nicholas P West, Alexander Brobeil, Jitendra Jonnagaddala, Nicholas Hawkins, et al. End-to-end prognostication in colorectal cancer by deep learning: a retrospective, multicentre study. *The Lancet Digital Health*, 6(1):e33–e43, 2024.

[12] Richard J Chen, Ming Y Lu, Drew FK Williamson, Tiffany Y Chen, Jana Lipkova, Zahra Noor, Muhammad Shaban, Maha Shady, Mane Williams, Bumjin Joo, et al. Pan-cancer integrative histology-genomic analysis via multimodal deep learning. *Cancer Cell*, 40(8):865–878, 2022.

[13] Nicolas Coudray and Aristotelis Tsirigos. Deep learning links histology, molecular signatures and prognosis in cancer. *Nature Cancer*, 1(8):755–757, 2020.

[14] Mingu Kang, Heon Song, Seonwook Park, Donggeun Yoo, and Sérgio Pereira. Benchmarking self-supervised learning on diverse pathology datasets. In *Proceedings of the IEEE/CVF Conference on Computer Vision and Pattern Recognition*, pages 3344–3354, 2023.

[15] Richard J Chen and Rahul G Krishnan. Self-supervised vision transformers learn visual concepts in histopathology. *arXiv preprint arXiv:2203.00585*, 2022.

[16] Sophia J Wagner, Daniel Reisenbüchler, Nicholas P West, Jan Moritz Niehues, Jiefu Zhu, Sebastian Foersch, Gregory Patrick Veldhuizen, Philip Quirke, Heike I Grabsch, Piet A van den Brandt, et al. Transformer-based biomarker prediction from colorectal cancer histology: A large-scale multicentric study. *Cancer Cell*, 41(9):1650–1661, 2023.

[17] Adalberto Claudio Quiros, Nicolas Coudray, Anna Yeaton, Xinyu Yang, Bojing Liu, Hortense Le, Luis Chiriboga, Afreen Karimkhan, Navneet Narula, David A. Moore, Christopher Y. Park, Harvey Pass, Andre L. Moreira, John Le Quesne, Aristotelis Tsirigos, and Ke Yuan. Mapping the landscape

of histomorphological cancer phenotypes using self-supervised learning on unannotated pathology slides, 2024. Accepted for publication.

[18] Jure Zbontar, Li Jing, Ishan Misra, Yann LeCun, and Stéphane Deny. Barlow twins: Self-supervised learning via redundancy reduction. In *International Conference on Machine Learning*, pages 12310–12320. PMLR, 2021.

[19] Maximilian Ilse, Jakub Tomczak, and Max Welling. Attention-based deep multiple instance learning. In Jennifer Dy and Andreas Krause, editors, *Proceedings of the 35th International Conference on Machine Learning*, volume 80 of *Proceedings of Machine Learning Research*, pages 2127–2136. PMLR, 10–15 Jul 2018.

[20] Chengkuan Chen, Ming Y Lu, Drew FK Williamson, Tiffany Y Chen, Andrew J Schaumberg, and Faisal Mahmood. Fast and scalable search of whole-slide images via self-supervised deep learning. *Nature Biomedical Engineering*, 6(12):1420–1434, 2022.

[21] Corentin Gueréndel, Phil Arnold, and Ben Torben-Nielsen. Creating small but meaningful representations of digital pathology images. In Manfredo Atzori, Nikolay Burlutskiy, Francesco Ciompi, Zhang Li, Fayyaz Minhas, Henning Müller, Tingying Peng, Nasir Rajpoot, Ben Torben-Nielsen, Jeroen van der Laak, Mitko Veta, Yinyin Yuan, and Inti Zlobec, editors, *Proceedings of the MICCAI Workshop on Computational Pathology*, volume 156 of *Proceedings of Machine Learning Research*, pages 206–215. PMLR, 27 Sep 2021.

[22] The cancer genome atlas program (tcga). https://www.cancer.gov/ccg/research/genome-sequencing/tcga. Accessed: 2023-05-09.

[23] Aimery de Gramont, Eric Van Cutsem, Hans-Joachim Schmoll, Josep Tabernero, Stephen Clarke, Malcolm J Moore, David Cunningham, Thomas H Cartwright, J Randolph Hecht, Fernando Rivera, et al. Bevacizumab plus oxaliplatin-based chemotherapy as adjuvant treatment for colon cancer (avant): a phase 3 randomised controlled trial. *The lancet oncology*, 13(12):1225–1233, 2012.

[24] Stéphanie M Zunder, Gabi W van Pelt, Hans J Gelderblom, Christoph Mancao, Hein Putter, Rob A Tollenaar, and Wilma E Mesker. Predictive potential of tumour-stroma ratio on benefit

from adjuvant bevacizumab in high-risk stage ii and stage iii colon cancer. *British Journal of Cancer*, 119(2):164–169, 2018.

[25] F Alexander Wolf, Fiona K Hamey, Mireya Plass, Jordi Solana, Joakim S Dahlin, Berthold Göttgens, Nikolaus Rajewsky, Lukas Simon, and Fabian J Theis. Paga: graph abstraction reconciles clustering with trajectory inference through a topology preserving map of single cells. *Genome biology*, 20:1–9, 2019.

[26] Herbert Hurwitz, Louis Fehrenbacher, William Novotny, Thomas Cartwright, John Hainsworth, William Heim, Jordan Berlin, Ari Baron, Susan Griffing, Eric Holmgren, et al. Bevacizumab plus irinotecan, fluorouracil, and leucovorin for metastatic colorectal cancer. *New England journal of medicine*, 350(23):2335–2342, 2004.

[27] Leonard B Saltz, Stephen Clarke, Eduardo Díaz-Rubio, Werner Scheithauer, Arie Figer, Ralph Wong, Sheryl Koski, Mikhail Lichinitser, Tsai-Shen Yang, Fernando Rivera, et al. Bevacizumab in combination with oxaliplatin-based chemotherapy as first-line therapy in metastatic colorectal cancer: a randomized phase iii study. *Journal of clinical oncology*, 26(12):2013–2019, 2008.

[28] Fairooz F Kabbinavar, Julie Hambleton, Robert D Mass, Herbert I Hurwitz, Emily Bergsland, and Somnath Sarkar. Combined analysis of efficacy: the addition of bevacizumab to fluorouracil/leucovorin improves survival for patients with metastatic colorectal cancer. *Journal of clinical oncology*, 23(16):3706–3712, 2005.

[29] Tessa P Sandberg, Maaike PME Stuart, Jan Oosting, Rob AEM Tollenaar, Cornelis FM Sier, and Wilma E Mesker. Increased expression of cancer-associated fibroblast markers at the invasive front and its association with tumor-stroma ratio in colorectal cancer. *BMC cancer*, 19(1):1–9, 2019.

[30] Gabi W van Pelt, Tessa P Sandberg, Hans Morreau, Hans Gelderblom, J Han JM van Krieken, Rob AEM Tollenaar, and Wilma E Mesker. The tumour–stroma ratio in colon cancer: the biological role and its prognostic impact. *Histopathology*, 73(2):197–206, 2018.

[31] Wilma E Mesker, Jan Junggeburt, Karoly Szuhai, Pieter de Heer, Hans Morreau, Hans J Tanke, and Rob AEM Tollenaar. The carcinoma–stromal ratio of colon carcinoma is an independent

factor for survival compared to lymph node status and tumor stage. *Analytical Cellular Pathology*, 29(5):387–398, 2007.

[32] Stéphanie Zunder, Priscilla Van der Wilk, Hans Gelderblom, Tim Dekker, Christoph Mancao, Anna Kiialainen, Hein Putter, Rob Tollenaar, and Wilma Mesker. Stromal organization as predictive biomarker for the treatment of colon cancer with adjuvant bevacizumab; a post-hoc analysis of the avant trial. *Cellular Oncology*, 42:717–725, 2019.

[33] Hideki Ueno, Yukihide Kanemitsu, Shigeki Sekine, Megumi Ishiguro, Eisaku Ito, Yojiro Hashiguchi, Fukuo Kondo, Hideyuki Shimazaki, Yoshiki Kajiwara, Koichi Okamoto, et al. A multicenter study of the prognostic value of desmoplastic reaction categorization in stage ii colorectal cancer. *The American journal of surgical pathology*, 43(8):1015–1022, 2019.

[34] Hideki Ueno, Yoshiki Kajiwara, Yoich Ajioka, Tamotsu Sugai, Shigeki Sekine, Megumi Ishiguro, Atsuo Takashima, and Yukihide Kanemitsu. Histopathological atlas of desmoplastic reaction characterization in colorectal cancer. *Japanese Journal of Clinical Oncology*, 51(6):1004–1012, 2021.

[35] Franck Pagès, Bernhard Mlecnik, Florence Marliot, Gabriela Bindea, Fang-Shu Ou, Carlo Bifulco, Alessandro Lugli, Inti Zlobec, Tilman T Rau, Martin D Berger, et al. International validation of the consensus immunoscore for the classification of colon cancer: a prognostic and accuracy study. *The Lancet*, 391(10135):2128–2139, 2018.

[36] Alexander Bagaev, Nikita Kotlov, Krystle Nomie, Viktor Svekolkin, Azamat Gafurov, Olga Isaeva, Nikita Osokin, Ivan Kozlov, Felix Frenkel, Olga Gancharova, et al. Conserved pan-cancer microenvironment subtypes predict response to immunotherapy. *Cancer cell*, 39(6):845–865, 2021.

[37] Jinru Shia, Nikolaus Schultz, Deborah Kuk, Efsevia Vakiani, Sumit Middha, Neil H Segal, Jaclyn F Hechtman, Michael F Berger, Zsofia K Stadler, Martin R Weiser, et al. Morphological characterization of colorectal cancers in the cancer genome atlas reveals distinct morphology–molecular associations: clinical and biological implications. *Modern pathology*, 30(4):599–609, 2017.

[38] C Richard Boland and Ajay Goel. Microsatellite instability in colorectal cancer. *Gastroenterology*, 138(6):2073–2087, 2010.

[39] Elisabeth J Kap, Petra Seibold, Swantje Richter, Dominique Scherer, Nina Habermann, Yesilda Balavarca, Lina Jansen, Natalia Becker, Katrin Pfütze, O Popanda, et al. Genetic variants in dna repair genes as potential predictive markers for oxaliplatin chemotherapy in colorectal cancer. *The pharmacogenomics journal*, 15(6):505–512, 2015.

[40] Gongmin Zhu, Lijiao Pei, Hongwei Xia, Qiulin Tang, and Feng Bi. Role of oncogenic kras in the prognosis, diagnosis and treatment of colorectal cancer. *Molecular cancer*, 20(1):1–17, 2021.

[41] Shih-Ching Chang, Pei-Ching Lin, Jen-Kou Lin, Chien-Hsing Lin, Shung-Haur Yang, Wen-Yi Liang, Wei-Shone Chen, and Jeng-Kai Jiang. Mutation spectra of common cancer-associated genes in different phenotypes of colorectal carcinoma without distant metastasis. *Annals of surgical oncology*, 23:849–855, 2016.

[42] Arthur Liberzon, Chet Birger, Helga Thorvaldsdóttir, Mahmoud Ghandi, Jill P Mesirov, and Pablo Tamayo. The molecular signatures database hallmark gene set collection. *Cell systems*, 1(6):417–425, 2015.

[43] Jakob Nikolas Kather, Johannes Krisam, Pornpimol Charoentong, Tom Luedde, Esther Herpel, Cleo-Aron Weis, Timo Gaiser, Alexander Marx, Nektarios A Valous, Dyke Ferber, et al. Predicting survival from colorectal cancer histology slides using deep learning: A retrospective multicenter study. *PLoS medicine*, 16(1):e1002730, 2019.

[44] Gabi W van Pelt, Sanne Kjær-Frifeldt, J Han JM van Krieken, Raed Al Dieri, Hans Morreau, Rob AEM Tollenaar, Flemming B Sørensen, and Wilma E Mesker. Scoring the tumor-stroma ratio in colon cancer: procedure and recommendations. *Virchows Archiv*, 473:405–412, 2018.

[45] Jianfang Liu, Tara Lichtenberg, Katherine A Hoadley, Laila M Poisson, Alexander J Lazar, Andrew D Cherniack, Albert J Kovatich, Christopher C Benz, Douglas A Levine, Adrian V Lee, et al. An integrated tcga pan-cancer clinical data resource to drive high-quality survival outcome analytics. *Cell*, 173(2):400–416, 2018.

[46] Carmen J Allegra, Greg Yothers, Michael J O'Connell, Saima Sharif, Nicholas J Petrelli, Linda H Colangelo, James N Atkins, Thomas E Seay, Louis Fehrenbacher, Richard M Goldberg, et al. Phase

iii trial assessing bevacizumab in stages ii and iii carcinoma of the colon: results of nsabp protocol c-08. *Journal of Clinical Oncology*, 29(1):11, 2011.

[47] Nicolas Coudray, Paolo Santiago Ocampo, Theodore Sakellaropoulos, Navneet Narula, Matija Snuderl, David Fenyö, Andre L. Moreira, Narges Razavian, and Aristotelis Tsirigos. Classification and mutation prediction from non–small cell lung cancer histopathology images using deep learning. *Nature Medicine*, 24, 2018.

[48] Erik Reinhard, Michael Ashikhmin, Bruce Gooch, and Peter Shirley. Color transfer between images. *IEEE Computer Graphics and Applications*, 21, 2001.

[49] Vincent A Traag, Ludo Waltman, and Nees Jan Van Eck. From louvain to leiden: guaranteeing well-connected communities. *Scientific reports*, 9(1):5233, 2019.

[50] Scott M Lundberg and Su-In Lee. A unified approach to interpreting model predictions. *Advances in neural information processing systems*, 30, 2017.

[51] Leland McInnes, John Healy, Nathaniel Saul, and Lukas Großberger. UMAP: Uniform Manifold Approximation and Projection. *Journal of Open Source Software*, 3(29), 2018.

[52] Aravind Subramanian, Pablo Tamayo, Vamsi K Mootha, Sayan Mukherjee, Benjamin L Ebert, Michael A Gillette, Amanda Paulovich, Scott L Pomeroy, Todd R Golub, Eric S Lander, et al. Gene set enrichment analysis: a knowledge-based approach for interpreting genome-wide expression profiles. *Proceedings of the National Academy of Sciences*, 102(43):15545–15550, 2005.